High-Precision Spectroscopy of Lead and Diatomic Molecules for Tests of Fundamental Physics

by
Charlene Peng

Professor Benjamin L. Augenbraun, Advisor
Professor Protik K. Majumder, Advisor

A thesis submitted in partial fulfillment
of the requirements for the
Degree of Bachelor of Arts with Honors
in Physics

WILLIAMS COLLEGE
Williamstown, Massachusetts
May 25, 2026

Abstract

This thesis presents advances in two complementary spectroscopy experiments, one molecular and the other atomic, unified by the common goal of probing physics beyond the Standard Model. We have upgraded a molecular beam spectroscopy apparatus, a versatile system capable of producing many metal-containing molecules and most recently used to perform hyperfine-resolved spectroscopy of dysprosium monoxide (DyO), with the addition of electric field plates. The installation of electric field plates enables observations of Stark-shifted spectra and consequently measurements of permanent molecular electric dipole moments, key quantities required to characterize candidate species for tests of fundamental physics. Separately, we have developed an experimental plan to demonstrate laser cooling in atomic lead (Pb) for the first time. Atomic lead (Pb) is a promising platform where parity nonconservation measurements may be improved, and lead-containing diatomic molecules such as AgPb and AuPb have recently been proposed as candidates for electron electric dipole moment (eEDM) searches. Our results mark progress toward the construction of the required laser system for laser cooling. Achieving laser cooling would mark an important step towards both improving resolution in ongoing atomic beam spectroscopy to benchmark lead (Pb) atomic theory and producing lead-containing molecules for future eEDM experiments.

Executive Summary

The Standard Model of particle physics is the most successful existing theoretical framework for describing the fundamental particles and interactions that govern the universe, yet it does not explain several major phenomena, including gravity, dark matter, and baryon asymmetry. Laboratory-scale "tabletop" experiments applying atomic, molecular, and optical (AMO) physics techniques provide a complementary approach to high-energy collider experiments in appraising the Standard Model. The work presented in this thesis marks experimental progress spanning two "tabletop" experimental platforms, both motivated by precision measurements of fundamental symmetry-violating interactions that benchmark the Standard Model.

A molecular spectroscopy apparatus in the Augenbraun Lab has been constructed to perform high-precision fluorescence spectroscopy of small metal-containing molecules that have been identified as especially sensitive probes to the existence of additional fundamental particles beyond the Standard Model. We expanded the spectroscopic capabilities of this apparatus with the addition of electric field plates, enabling the application of controlled electric fields within the fluorescence detection region.

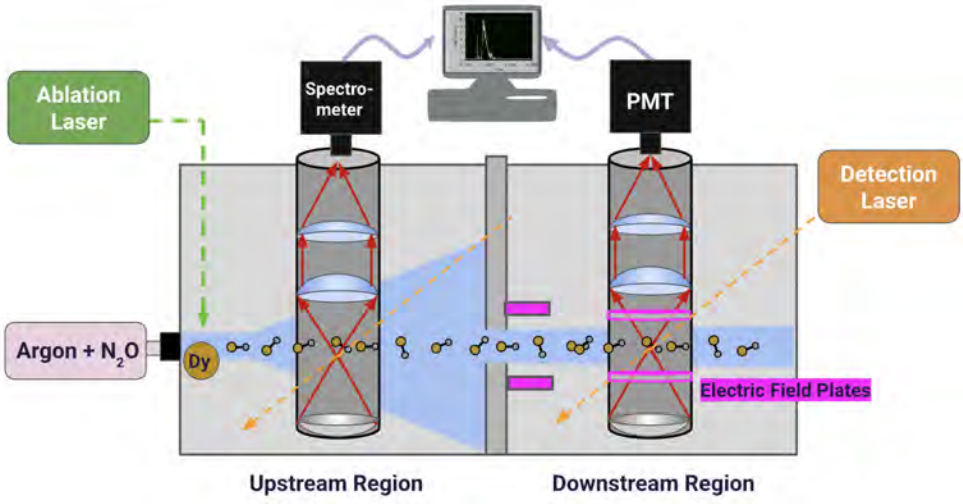

Figure 1: Schematic diagram of our upgraded molecular spectroscopy vacuum chamber. Components added for Stark shift measurements are displayed in pink. Figure adapted from Kendall Rice '25. [1]

This upgrade allows for the observation of Stark-shifted spectra, which are prerequisites for the measurement of molecular electric dipole moments and can also aid in the analysis of complicated spectra. To calibrate and test the electric field plates, we recorded Stark-shifted spectra for dysprosium monoxide (DyO), a molecule previously characterized in our experimental apparatus with a known electric dipole moment.

We have separately contributed to the development of a laser system for a first demonstration of laser cooling in atomic lead (Pb). Transverse cooling of the lead (Pb) atomic beam in the Majumder Lab has the possibility to yield new measurements of atomic parity non-conservation. Furthermore, lead (Pb) appears in many of the metal-containing molecules of interest to the Augenbraun Lab, and obtaining a laser-cooled sample of lead (Pb) is essential for producing these lead-containing molecules.

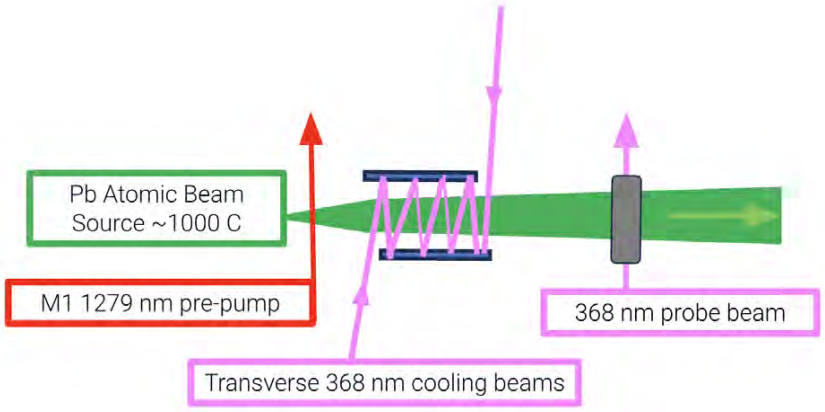

Figure 2: Sketch of the planned experimental framework for demonstrating transverse laser cooling in atomic lead (Pb). The experiment is built around three primary objectives: generating a lead atomic beam, implementing laser cooling using optical cycling transitions, and imaging the cooled beam to verify transverse cooling. A major component of this thesis is the development of a new ultraviolet laser source for the second objective.

Achieving laser cooling requires roughly 100 mW of laser light at 368 nm. Existing 368 nm external cavity diode laser systems in the laboratory are sufficient for atomic beam spectroscopy but do not provide enough optical power for efficient cooling. We have designed a new laser source to produce 100 mW of 368 nm light by doubling the frequency of 736 nm light from a titanium-sapphire (Ti:Sapph) laser with a nonlinear crystal in a resonant cavity. The main body of experimental work for this project involved aligning and stabilizing the frequency of the Ti:Sapph laser. We confirmed a maximum of roughly 400 mW of single-frequency radiation from the Ti:Sapph and demonstrated that the frequency can be stabilized through PID control. We also obtained a new non-linear crystal for our bow-tie frequency doubling cavity. While this progress provides a critical foundation for the experimental infrastructure required for laser cooling, additional work remains to be done to optimize the laser's output power and achieve efficient second harmonic generation.

Acknowledgments

First and foremost, I am deeply grateful to my thesis advisors, Professor Ben Augenbraun and Professor Tiku Majumder. You have both taught me an immense amount and have profoundly shaped my desire to continue pursuing physics. Tiku, your excitement for teaching shone through in PHYS 142, and I may not have been a physics major had I not had you as an example of how passionate the professors in the department are committed to supporting their students. Ben, it has been such a rewarding experience to have been involved in your lab from the early days. The enthusiasm and positivity you bring to your research and to advising has made me similarly excited, and I have been sincerely grateful for your support every step of the way.

Thank you also to my second reader, Professor Charlie Doret, who I've been lucky to learn from in many courses, and who has challenged me in each one to further my understanding and become a better physicist.

Finally, I am grateful to my family for being such a steady source of guidance and support. I am grateful to all of my fellow physics majors, friends, coaches, and teammates here at Williams who have made campus such a special place. You all are simply the best, and it's difficult to find the right words to express just how lucky I am!

Contents

List of Figures

Chapter 1

Introduction

On March 13, 1781, astronomer William Herschel discovered Uranus, the seventh planet from the Sun, while observing the constellation Gemini [2]. This discovery occurred after Isaac Newton formulated his laws of motion and universal gravitation, which enabled astronomers to predict the motion of the six other known planets in our solar system at the time. However, continued observations of Uranus revealed irregularities in the planet's orbit that contradicted calculations based on Newton's laws. To account for these discrepancies, astronomers hypothesized the existence of a more distant, unseen planet whose gravitational influence would have caused the observed perturbations to Uranus' orbit. In 1845, two astronomers independently calculated the location of this postulated planet. Neptune was discovered just one year later, observed only one degree away from its calculated position [3].

The discovery of Neptune exemplifies the powerful dialogue between measurement and theory that is ubiquitous in physics. Precise measurements reveal anomalies. Theory is created to explain them, generating new testable predictions in the process. New observations then confirm or challenge those predictions, catalyzing even further theoretical propositions in a continuous cycle that drives science forward.

Over the past few centuries, this dynamic interplay between empirical evidence and mathematical reasoning has culminated in the Standard Model of particle physics. At each stage, this cycle introduced new physics that repeatedly reshaped our understanding of the world we live in, from the mechanics of planetary motion, to the structure of space and time, to the behavior of matter at the most fundamental level.

1.1 Beyond the Standard Model

The Standard Model is a Quantum Field Theory (QFT), a framework in modern physics that describes subatomic particles as quantized, localized energetic excitations (ripples) in fields that permeate all space, with each particle having a corresponding underlying field. The Standard Model consists of 17 fundamental particles, divided into two primary classes, fermions (matter particles) and bosons (force carrier particles) [4]. Since its invention in

the 1970s, the model has successfully predicted the existence of every particle detected, and has explained almost all interactions between them. For example, electrostatic interactions between electrons (a type of fermion) are mediated by emission and absorption of photons, the electromagnetic force-carrying bosons [5]. The 2012 observation of the predicted Higgs Boson marked a significant milestone for the Standard Model in confirming the existence of the Higgs field, which allows particles to have mass [6]. However, the Standard Model has been described not only as the great success of modern physics, but also as the great frustration [7]. Its failure to account for cosmological phenomena such as gravity, baryogenesis, and dark matter confirm that the model remains incomplete.

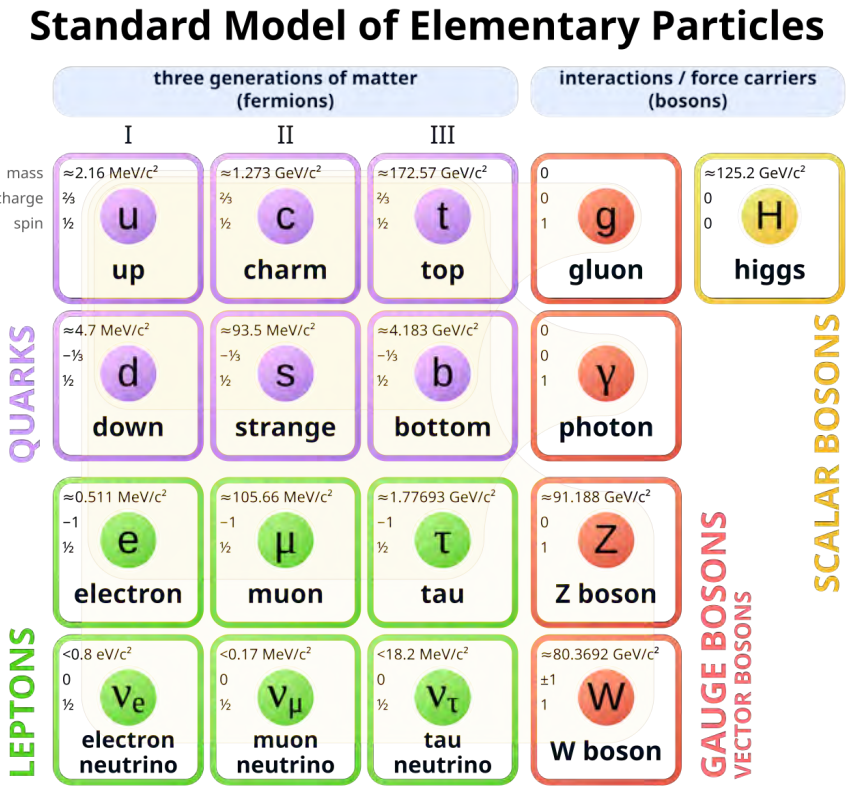

Figure 1.1: Particles of the Standard Model. Figure made by Cush, Public Domain, via Wikimedia Commons.

Gravity and The Hierarchy Problem

Physicists have designated four fundamental forces that govern the universe: strong, electromagnetic, weak, and gravitational. These forces are differentiated by their strength and range. The strong forces bind subatomic particles together in the nucleus of atoms. Electromagnetic forces comprise most of the forces observable in our every day lives —

friction,"normal" force, even the chemical forces holding molecules together. Weak forces are short range, accounting for specific types of radioactive decay. The gravitational force pales in strength in comparison to the other three, but works at infinite range [8]. The Standard Model unifies the first three of these fundamental forces but fails to incorporate gravity, leaving the relative weakness of gravitational forces (the hierarchy problem) an open theoretical challenge.

Baryogenesis

Our universe is dominated by matter rather than antimatter. This is a fact that enables our very existence — otherwise, the matter that makes up our world would have annihilated with its antimatter counterpart long ago. This "baryon asymmetry" in the universe is a fact that the Standard Model cannot explain. The matter remaining in the universe today is estimated to comprise around one-billionth of all the particles created at the Big Bang, as the rest of the original particles have collided with their antimatter partners. The Standard Model does generate a baryon asymmetry, but its prediction of the quantity of remaining particles is significantly smaller than experimentally determined values. Theories extending beyond the Standard Model improve these projections by introducing new particles and forces [6].

Dark Matter

The nature of dark matter presents another gap in the Standard Model. While the Standard Model provides an adequate description of the early universe shortly after the big bang in terms of quarks and pair production, cosmological observations indicate that our universe contains significantly more mass and energy than has been detected. This additional mass and energy are referred to as dark matter and dark energy, since they are not observable through interactions with light. Numerical simulations, which predict how matter evolved under the force of gravity in the expanding universe, not only reveal how dark matter particles play a significant role in defining large scale structure but also provide insight into the likely form of dark matter particles, particularly whether their effects were relativistic (hot) or non-relativistic (cold). Simulations indicate that standard model neutrinos, which are the only viable Standard Model particles for dark matter due to their relative stability and lack of electromagnetic interactions, are too light and too hot to be the primary component of dark matter [9]. Instead, cold dark matter is estimated to be around 10 times as abundant as baryonic matter in our universe [10]. Today, particle physicists continue to search for this unknown particle species.

The Strong CP Problem

Until the 1950s, physicists believed that the laws of physics were identical for a system and for its mirror image — parity was always conserved. This assumption changed when the 1957 Nobel Prize winners Lee and Yang [11] proposed that parity violation may exist

in the electroweak force, a postulate experimentally confirmed by Wu in observations of nuclear beta decay [12]. Alongside parity inversion (P), physicists also consider symmetry under charge conjugation (C), which replaces particles with antiparticles, and time reversal (T), which compares interactions going forward and backward in time. In the Standard Model, C, P, and T are all conserved for electromagnetic interactions. For electroweak and strong interactions C, P, and T violations are permitted individually and in pairs, but not all together (CPT invariance) [13]. For example, CP symmetry violations, which are necessary to account for the universe's baryon asymmetry, must be paired with T symmetry violations to ensure that total symmetry remains unchanged [6].

Although CP symmetry violations are allowed in both the weak and strong forces, they have only been observed in electroweak interactions. This mystery of why CP symmetry violations have not been observed in strong interactions when the Standard Model predicts otherwise is known as the strong CP problem [13]. Even when incorporating all CP symmetry violations mathematically allowed, the magnitude of CP symmetry breaking predicted by the Standard Model falls short of the quantity necessary to account for the baryon asymmetry observed in our universe today. This indicates that there must be greater CP symmetry violations in nature, the sources of which are speculated in nearly all extensions to the Standard Model [6, 14].

1.2 Tabletop Experiments

The most widely publicized approaches to the search for physics beyond the Standard Model (BSM) are large, resource intensive collaborations, such as the Large Hadron Collider (LHC) at CERN. However, the expanding atomic, molecular, and optical (AMO) physics toolbox of stable lasers and novel trapping techniques have also enabled probing of physics beyond the Standard Model in smaller scale "table-top" experiments, through the precise control and observation of the quantum behavior of atoms and molecules [6].

1.3 Spectroscopy, Optical Cycling and Laser Cooling

Symmetry violations relevant to fundamental physics can be encoded in small shifts in the discrete energy levels of atoms and molecules. The quantized atomic and molecular energy levels described by quantum mechanics have been studied for centuries in the field of spectroscopy, which investigates absorption, emission, and scattering interactions when light is incident upon matter. In the discipline's evolution from early observations employing sunlight dispersed by a prism to modern laser-based precise measurements, spectroscopy has yielded a preponderance of our knowledge of atoms and molecules [15]. Not only did the advent of the laser in 1960 enable higher resolution and greater sensitivity in spectroscopy as a narrow-bandwidth, intense, and highly tunable light source, it also paved the way for novel techniques to trap atoms and molecules [15, 16].

Trapping atoms and molecules is synonymous with cooling them, since the temperature of a gas is a measure of the average speed of the particles in the gas, with temperature growing quadratically with average speed. Doppler cooling, facilitated by the high intensity light produced in laser technology, is a common method by which millikelvin temperatures can be achieved. Doppler cooling is predicated on Einstein's prediction that photons not only possess energy, but also carry momentum. Then, by conservation of momentum, when an atom or molecule absorbs a photon traveling from the opposite direction, the speed of the atom (which is now in a higher energy state) is reduced. Importantly, the Doppler shift phenomenon makes it so that the wavelength an atom or molecule perceives a photon to be depends on its velocity relative to the photon's. If an atom or molecule and a photon are moving towards each other, the atom or molecule will perceive the photon as having a shorter wavelength than if they were moving in the same direction. Since energy levels are quantized, by using laser light slightly red-shifted from the transition frequency, one can target atoms or molecules moving at a particular (high) velocity in the direction of laser propagation. Only the atoms or molecules moving at the high velocity will see the photons in the beam at the transition frequency and absorb them, slowing down in the process. Eventually, the absorbed photon is spontaneously emitted in a random direction. Although it is possible that the photon may be emitted along the direction of laser beam propagation, it is unlikely that this will happen for every photon absorbed and re-emitted. Using this scheme, high power laser light can generate a net cooling effect for the atoms or molecules in the direction parallel to the direction of its propagation.

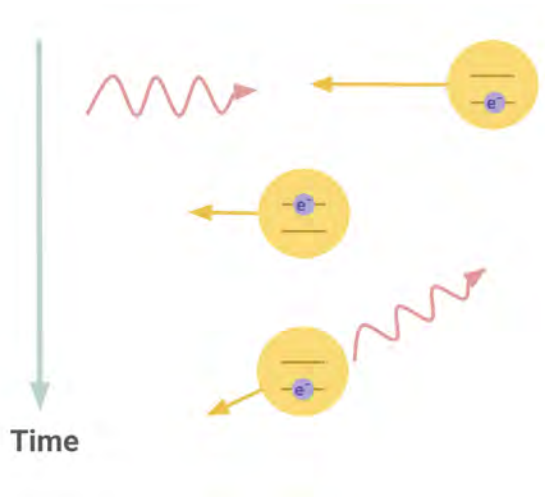

Figure 1.2: Diagram of Doppler cooling. An atom absorbs a photon red-detuned from resonance moving in the opposite direction. As a result, the atom is slowed and excited. The photon is then re-emitted in a random direction during spontaneous decay.

High power laser light is essential because the momentum of photons is small relative to that of atoms and molecules. Therefore, in order to significantly slow and cool an atom or molecule, the absorption and re-emission processes (optical cycling) must occur many times. Some atoms and molecules are more well-suited for efficient optical cycling than others. Effective optical cycling requires a transition in which the lifetime of the excited state is relatively short to enhance the speed of cooling, and in which the atom or molecule will most likely return to its original energy state after spontaneous decay so that it can be excited again by the same laser.

One motivation for laser cooling is that colder samples yield more precise spectroscopic measurements. Atoms or molecules moving at different speeds within the sample view the

detection laser frequency differently and absorb photons slightly red and blue of the true transition frequency. This generates a cumulative effect of broadening in the observed line that can be attenuated by cooling the sample and reducing the distribution of speeds.

1.3.1 Atomic Parity Non-Conservation

Improved laser technologies and techniques have aided in the probing of fundamental symmetries in "tabletop" experiments. Investigating parity non-conservation (PNC) in atomic systems has remained an active area of interest for AMO physicists. PNC increases with nuclear charge Z, scaling roughly as Z^3, and is therefore more pronounced in heavy atoms. Atomic systems in which PNC effects have been measured include cesium, ytterbium, bismuth, thallium, and lead [14].

Atomic parity violation experiments complement high-energy physics experiments as one of the most precise probes of the low-energy electroweak of the Standard Model. Experiments operating in this low-energy regime are sensitive to weak effects that may be negligible and difficult to detect in high-energy experiments. Thus, atomic parity non-conservation experiments are particularly well-suited for searches additional dark force carriers (gauge bosons) and for dark matter candidates such as axions [14]. Axions and axion-like particles have additional relevance as proposed solutions to the strong CP problem [6, 17].

1.3.2 Electric Dipole Moments

CP symmetry violations manifest as permanent electric dipole moments (EDMs) in subatomic particles and can therefore be investigated by laboratory-scale AMO experiments. The existence of a permanent electric dipole moment inherently breaks T-symmetry since upon time reversal, the static charge distribution remains constant but the spin reverses direction (Figure 1.3). Assuming CPT invariance, the presence of T-symmetry violations implies accompanying CP symmetry violations. The greater the CP-violating interaction, and the smaller the new particles that carry it, the larger the EDM predicted for an elementary particle that is affected by it. EDMs for electrons and nuclei are associated with different proposed forces, so searches for both have the potential to inform particle physics [6].

Recent electron electric dipole moment (eEDM) measurements, particularly those performed by the ACME collaboration and researchers at JILA, have placed some of the strongest experimental constraints on physics beyond the Standard Model. One common type of theory used to predict CP-violating interactions are supersymmetric (SUSY) theories, in which every Standard Model particle has a corresponding "superpartner" with different spin statistics. Many SUSY theories predict an eEDM large enough to be observed with modern precision spectroscopy techniques. However, the continued absence of a detected eEDM in these experiments have excluded broad regions of supersymmetric parameter space. Even while measuring "zero" these precision eEDM experiments have become powerful probes of new physics, significantly constraining viable extensions of the Standard Model.

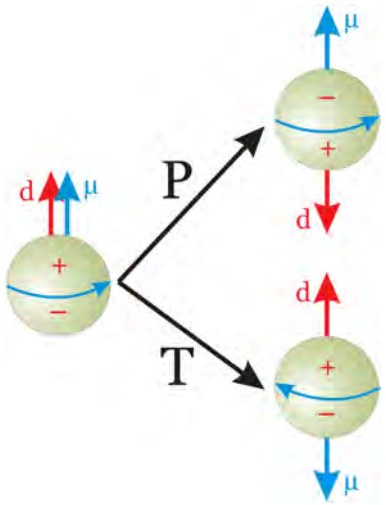

Figure 1.3: Electric dipole moment causes P and T Violation. When a particle begins with an electric dipole moment oriented on the same axis of its spin, the relative directions of these two vectors change under both time reversal (T) and parity inversion (P), requiring a similar change under charge conjugation (C) in order to preserve CPT invariance. Andreas Knecht, Public domain, via Wikimedia Commons.

1.4 Thesis Overview

In the spirit of these landmark experiments, both the Augenbraun Lab and Majumder Lab use atomic and molecular systems as platforms for precise spectroscopic measurements of beyond Standard Model (BSM) physics. This thesis describes progress towards production, spectroscopy, and laser cooling of atoms and molecules in these two different tabletop experiments at Williams College. In Chapter 2, we describe a molecular spectroscopy apparatus used to perform hyperfine-resolved spectroscopy of dysprosium monoxide (DyO) in the Augenbraun Lab. We discuss an extension to this apparatus, with the design of electric field plates to enable electric dipole moment measurements. Chapter 3 introduces the motivation and experimental plan for a collaborative effort in the two groups to demonstrate laser cooling in atomic lead (Pb) for the first time. We detail the experimental progress made towards developing a laser system for this application. Finally, Chapter 4 synthesizes the results and outlines recommended directions for future investigation.

Chapter 2

Electric Field Plates for Stark Shift Spectroscopy

A central motivation of the Augenbraun Lab is the spectroscopic study of metal-containing diatomic molecules that are particularly viable for probing fundamental symmetries. By elucidating energy levels through high-precision fluorescence spectroscopy, we aim to improve models of molecular bonding and characterize candidate molecules for laser control and precision measurement.

Recently, we produced and examined dysprosium monoxide (DyO), a molecule displaying enhanced sensitivity to BSM physics in the search for the Nuclear Schiff Moment [18]. Other species we are interested in examining include diatomic molecules comprised of a coinage metal element (Cu, Au, Ag) and a group 14 element (C, Si, Ge, Sn, Pb). Many of these molecules have been identified as promising candidates for optical cycling and precision searches for the electron's electric dipole moment (eEDM), making them viable probes of physics beyond the Standard Model [19].

2.1 Molecular Spectroscopy Experimental Overview

Many of the molecules we are interested in are unstable and therefore commercially unavailable, so they must be produced in the lab. We designed and built a pulsed supersonic molecular beam source in vacuum to synthesize these metal-containing molecules and perform high-precision fluorescence spectroscopy of them. This is a widely used synthesis method to generate molecules in the gas phase at temperatures on the order of 10 K. In this approach, a reagent gas mixture flows into our vacuum chamber through a pulsed valve and cools as it undergoes adiabatic expansion. A pulsed laser then ablates a nearby metal target, producing vaporized metal atoms that react with the expanding gas to form our molecules, which travel through our cavity in a beam.

To create a spectrum, we scan the frequency of a detection laser traveling through our molecular beam. When the energy of the laser light coincides with the energy of a transition in molecules, the molecules absorb photons and become excited. Identifying which wave-

lengths are absorbed by the molecular beam reveals key information about the structural properties of the molecules, since absorption corresponds directly to specific energy gaps. One common method of spectroscopy, absorbance spectroscopy, monitors the amount of light traveling through the sample to locate the molecules' transitions. However, in our experiments, we apply a different technique, capturing the dispersed laser-induced fluorescence (DLIF) as the excited molecules spontaneously decay to lower energy states. This method, known as fluorescence spectroscopy, offers greater sensitivity than absorbance spectroscopy because it measures a non-zero signal against a dark background, rather than detecting small dips in a high-intensity background.

Ultimately, our spectroscopic analysis aims to elucidate the molecular hyperfine structure arising from interactions between nuclear spin and surrounding electromagnetic fields due to electron orbit, spin, and angular momenta. Molecular energy levels vary according to their electronic, vibrational, and rotational states. The largest energy differences arise from electronic structure, while the smallest come from rotational motion. Additional splitting of energy levels occur due to electron spin–orbit coupling, referred to as fine structure, and even subtler variations are introduced by hyperfine structure. Detecting these small energy shifts requires resolution on the order of 0.003 cm^{-1}. In our experiment, we can achieve a resolution of about 7 $\times 10^{-4}$ cm^{-1}.

Further details of our molecular spectroscopy experimental apparatus are described in the theses of Cooper Stuntz '24, Kendall Rice '25, and Nicole Albright '25. In this chapter, I provide an overview of the experimental setup and describe in detail my contributions to it, which primarily relate to molecule synthesis, software for experiment control. Then, I highlight an expansion of the experimental capabilities through an upgrade to the system that enables the application of an external electric field and the measurement Stark-shifted spectra.

2.2 Molecule Synthesis

During the synthesis process, a pulsed valve first opens, allowing a reagent gas mixture to flow into the vacuum chamber. A pulsed laser then enters the vacuum chamber from above, ablating a metal target mounted just downstream of the pulsed valve. The vaporized metal atoms form a reactive plasma that combines with the reagent gas mixture to produce any possible combination of the constituents. We can ensure that our molecules of interest are among the species produced by changing the content of the reagent gas and metal target. For instance, we use a high-purity dysprosium (Dy) target

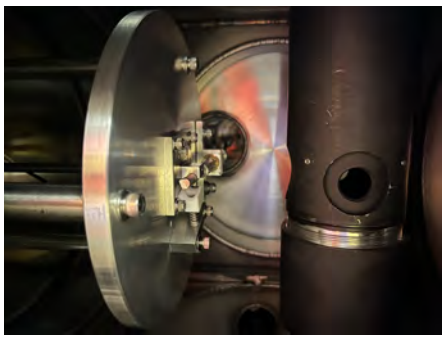

Figure 2.1: Photograph of Metal Target Mounted in Vacuum Chamber

and introduce a gas mixture of nitrous oxide Nx_2O in argon to produce DyO molecules. As the molecular beam expands, it cools adiabatically.

Our ablation laser, a pulsed Neodymium: Yttrium Aluminum Garnet (Nd:YAG) laser, produces a beam with a diameter of approximately 6 mm. This diameter is too large for effective ablation at the target, which is typically a 6.3mm diameter tube or cylinder around 5 cm long. An optics setup incorporating mirrors, a plano-concave lens, and two plano-convex lenses directs the beam from the ablation laser onto the target (Figure 2.2). The plano-concave (negative) lens works in conjunction with the plano-convex (positive) lens to collimate the beam. By adjusting the path length from the final positive lens to the target, we can adjust the focal point so that the beam reaches a focus at the target.

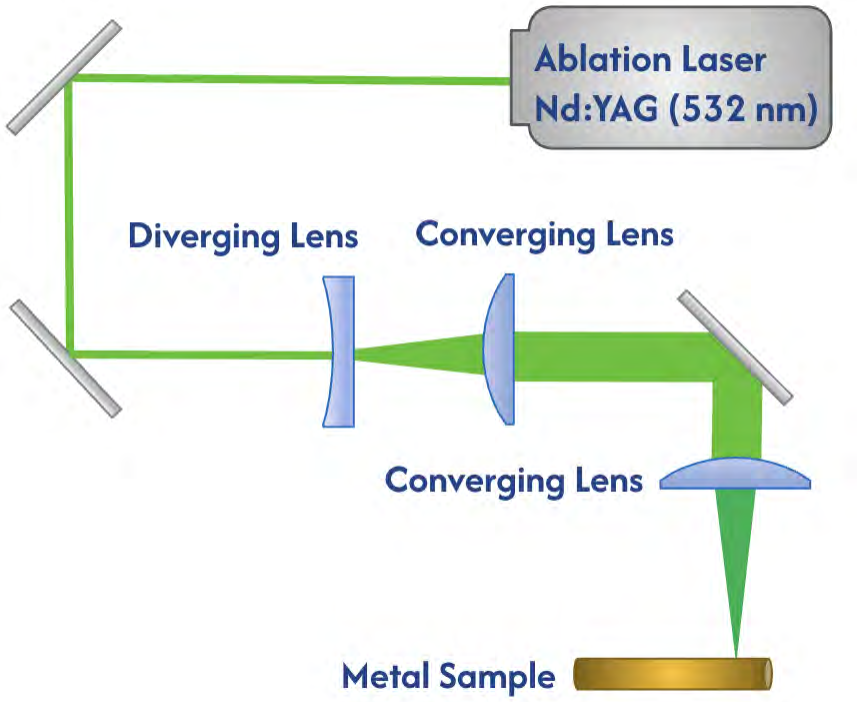

Figure 2.2: Optical setup for expansion, collimation and focus of ablation laser beam. Mounted above the experiment, the ablation laser beam descends vertically into the vacuum chamber through a window on the ceiling of the chamber and must be focused on the metal target for effective ablation.

Each pulse from the ablation laser vaporizes metal at the point where the beam comes in contact with our target. Therefore, to maintain consistent ablation yields, we must rotate and translate our target to adjust the ablation location after each pulse of the laser. This adjustment is done with a fine thread screw and flexible shafts both inside and outside the vacuum chamber, which are rotated by a stepper motor mounted outside of the chamber. The stepper motor is programmed for computer control through NI LabVIEW. Circuits to

convert 5V pulses from our computer into 24V pulses for input signaling to the motor are enclosed in a box, described in Appendix A.1, where BNC compatible inputs and outputs are available for communication with our computer.

2.3 Laser-Induced Fluorescence Spectroscopy

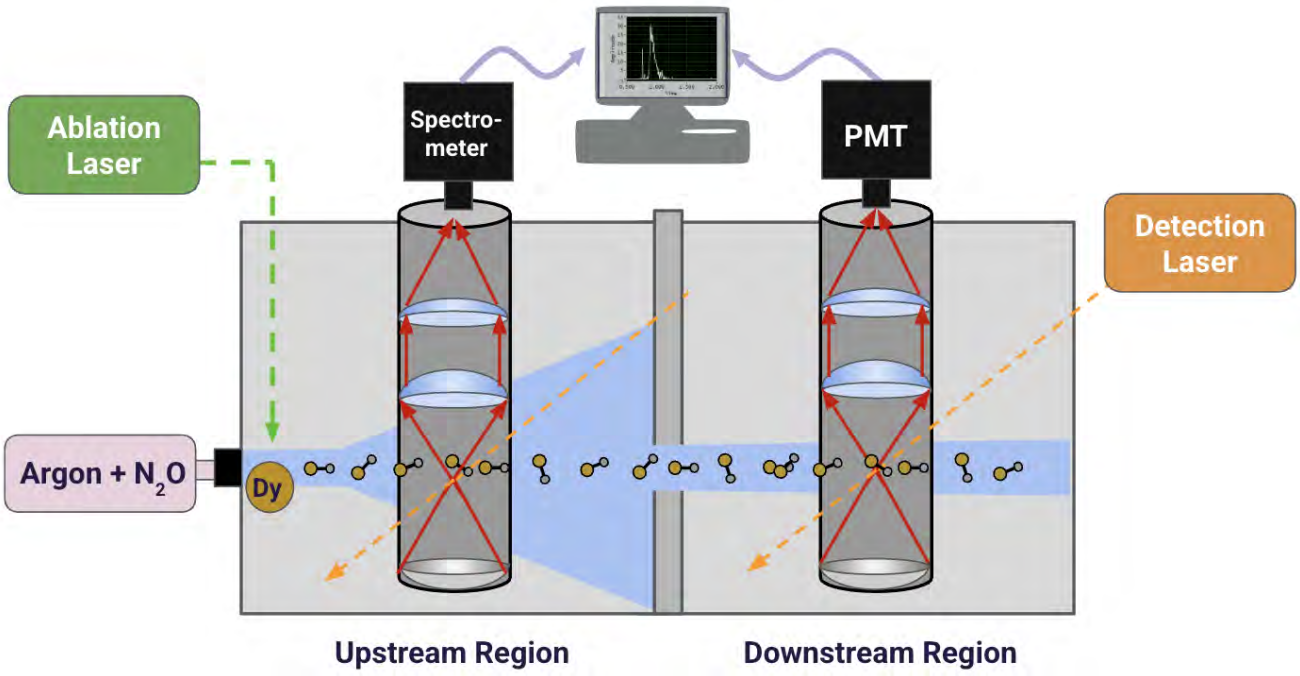

Figure 2.3: Schematic diagram of our molecular spectroscopy vacuum chamber. Figure adapted from Kendall Rice '25. [1]

We can perform fluorescence spectroscopy at either of two detection sites, one in the upstream region of our vacuum chamber and one in the downstream region. We only operate in one site at a time. There is an aperture between these two regions that allows only the collimated component of the molecular beam to pass through, allowing for higher resolution at the downstream site by reducing Doppler broadening. At each detection site, there is a set of collection optics (Figure 2.4 to direct the laser-induced fluorescence to our light detection tools — a photomultiplier tube (PMT) or a spectrometer.

At the upstream detection site, a higher number of molecules, and thus a larger signal, are accompanied by more background and lower resolution. The elevated background occurs because this detection site is close to the site of molecule production, which leads to chemiluminescence and stray light from impurities[1]. Typically, we use a spectrometer at this

[1]In our case, these impurities are any species that are not our desired molecule. These may well be new

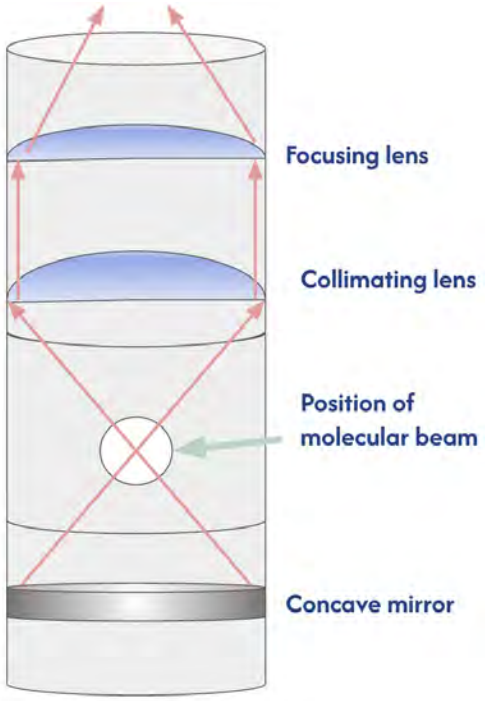

Figure 2.4: Diagram of optics to collect DLIF. Figure adapted from Kendall Rice '25. [1]

site to measure the frequency of emitted light. Since the highest achievable resolution of the spectrometer is approximately 2 cm-1, we primarily use a pulsed detection laser at this site to locate electronic transitions when identifying new molecules.

There are fewer molecules and a smaller signal at the downstream detection site as a result of the aperture. However, this site benefits from less noise and higher resolution. Here, we use a photomultiplier tube (PMT) to record the intensity of emitted light and probe molecules using a single frequency continuous-wave laser for a narrow spectrum. Since the PMT is sensitive enough to detect single photons, we can perform off-diagonal detection — collecting fluorescence at a wavelength different from the excitation wavelength — eliminating potential laser scatter. This downstream site is where we can accomplish the aforementioned resolution of about 7 $\times 10^{-4}$ cm^{-1} that surpasses the threshold for resolving hyperfine structure.

We designed our detection regions to be compatible with multiple types of detection lasers. Our ability to swap detection lasers is valuable because different lasers have advantageous features for different parts of the spectroscopy process. For our lower resolution spectroscopy to identify electronic transitions at the upstream detection site, we select a detection laser with a wide linewidth. Our most suitable options are our optical parametric oscillator (OPO) or our pulsed dye laser. The OPO, a Radiant Tunable Laser produced by Opotek Lasers, is actually not a laser since it does not use stimulated emission to generate radiation. Instead, the OPO uses parametric amplification to create optical gain across

unstudied molecules with exciting properties and applications. One man's trash is another man's treasure.

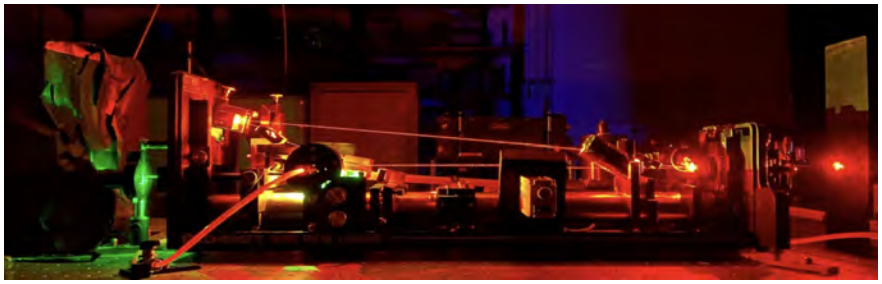

Figure 2.5: Photograph of our Coherent 899 CW Dye Ring Laser in operation. The laser's wide tunability throughout the visible region and narrow linewidth make it advantageous for high-resolution spectroscopy.

multiple frequencies. It employs a non-linear crystals to convert a single pump laser beam into two lower-frequency beams through second-order nonlinear interactions.[2] The OPO is widely tunable and can output wavelengths from 410 nm – 710 nm. Each output pulse has a bandwidth of about 100-200 GHz, making it the option with the broadest linewidth. Our pulsed dye laser, a Sirah Lasertechnik Cobra-Stretch, has a bandwidth around 2 GHz, which is significantly narrower. Due to its higher resolution, the pulsed dye laser is capable of revealing certain rotational structures that the OPO cannot.

To resolve hyperfine structure, which we typically do at the downstream detection site, we use a continuous-wave (CW) Coherent 899 dye ring laser. The CW dye laser is tunable in the visible region between roughly 550-700 nm, depending on the dye mixture used as the gain medium. The CW dye laser's narrow stabilized linewidth of around 1 MHz makes it well-suited for high-resolution spectroscopy.

2.4 Experiment Control

The synthesis of molecules, the scanning of detection lasers, and the collection of laser-induced fluorescence during high-resolution spectroscopy all occur on microsecond timescales, synchronized in an NI LabVIEW program. The program allows users to set parameters for data acquisition, including the range of frequencies to scan the detection laser, the number of ablation laser shots for which the detection laser should stay at one frequency, and the rate at which molecules should be synthesized. The program displays a graph of the data from the light detectors as it is collected, and has capabilities to show processed (background subtracted, normalized, integrated, and filtered) data (Figure 2.6). The program exports collected data alongside scan parameters to the computer for more detailed analysis later on. Further details regarding this program are contained in Appendix B.2.2.

[2] A brief overview of non-linear optics is provided in Section 3.2

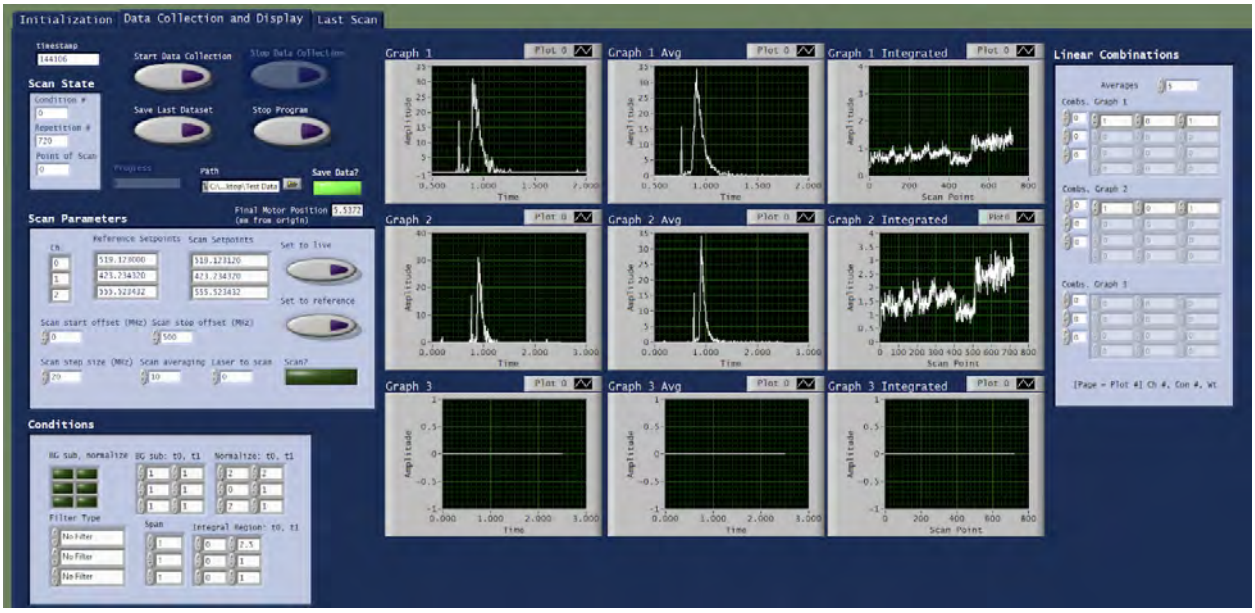

Figure 2.6: Front end of experimental control and data acquisition LabVIEW program after data collection

2.5 Motivating Stark Shift Measurements

The natural world is extraordinarily complex, with countless interconnected processes and interactions spanning from subatomic scales to entire ecosystems. As an effort to disentangle this complexity and discern underlying relationships, experimental science seeks to reproduce and test natural phenomena in controlled environments. Although perhaps more obvious in disciplines where experiments address causation and independent and dependent variables are more explicitly outlined, this guiding principle is reflected in our work as well. We go through the effort to produce our molecules in vacuum to isolate them from the outside environment. With our cryogenic buffer-gas system, we have controlled the temperature of our molecules, simplifying spectra by forcing our molecules into the ground vibrational state and the lowest angular momentum states. To extend our experimental apparatus, another valuable parameter to control is the external electric field experienced by the molecules.

Our molecules of interest are electrically neutral. In the presence of an external electric field, the interaction between the induced or permanent electric dipole of the molecules lead to energy level shifts. This is known as the Stark effect, and the energy level shifts are referred to as Stark shifts. For molecules with permanent electric dipole moments, energy shifts depend on how that dipole is oriented in the field. In the simplest case, the shift is linear:

$$\Delta E \ -\vec{d}\cdot\vec{E}$$

where $\vec{d}$ is the permanent dipole moment and $\vec{E}$ is the electric field. The presence of the external electric field can also polarize molecules, leading to an induced dipole moment $\vec{d}_{ind} = \alpha\vec{E}$ where α is the polarizability of the molecule. This induced dipole moment brings

a quadratic contribution to the Stark effect:

$$\Delta E = -\frac{1}{2}\alpha E^2$$

[20].

Thus, measurement of Stark shifts informs molecular structure by revealing the molecule's intrinsic electric dipole moment and polarizability. Inducing Stark shifts is also useful for identifying peaks in complicated spectra. Different quantum states shift by different amounts, so applying an electric field can help separate, label, and selectively address transitions that might otherwise overlap.

2.6 Electric Field Plate Design

In order to make Stark shift measurements, we need to design electric field plates that are compatible with the detection region of our vacuum chamber.

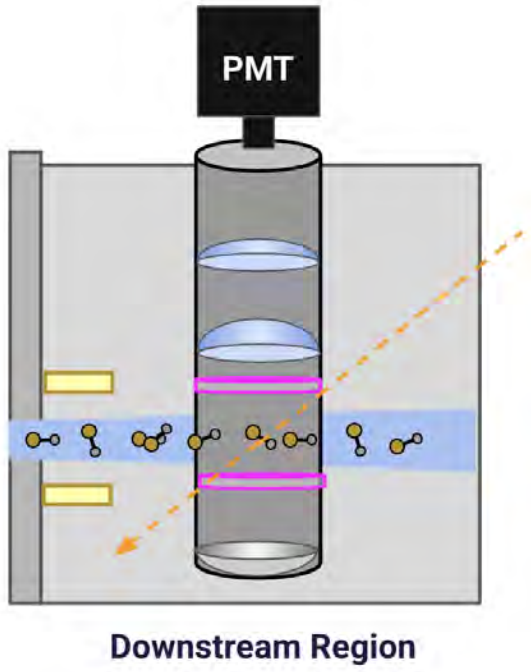

Figure 2.7: Schematic diagram of molecular spectroscopy vacuum apparatus with electric field plates shown in pink. An additional set of electric field plates, shown in yellow, were added later to remove ions from the molecular beam.

We aim to generate electric fields on the order of a few kilovolts per centimeter, which corresponds to applied voltages of roughly 5 kV depending on the separation between the plates. Achieving this safely requires careful insulation and consideration of the effects of

fringing fields. We also need to select vacuum-compatible materials in order to maintain the integrity of our vacuum.

A unique design challenge here is that the plates need to be transmissive to allow for fluorescence detection. Furthermore, our existing collection optics setup were not designed with electric field plates in mind. The collection optics we use for fluorescence detection are mounted in cylindrical tubes that are 2 inches in diameter. To maintain a uniform electric field at the detection site, we select electric field plates 2 inches in diameter as well. However, because the plates require insulation, they cannot be installed using our existing tubes. We must devise an alternative solution to mount them in the vacuum chamber.

We handle the first of these design challenges by using transmissive glass thinly-coated with a conducting metal for our plates. It turns out this type of material is commercially available in the form of ThorLabs neutral density (ND) filters, which are typically used to attenuate the intensity of laser beams. The ThorLabs N-BK7 Reflective ND filter series uses an N-BK7 glass substrate with a metal (Inconel) coating deposited on one side. Inconel is a nickel and chromium based metallic alloy. Although not as conductive as aluminum or copper, it is is still electrically conductive [21]. Since we want the electric field plates to be as transmissive as possible, we tested ND filters to identify the model with minimal attenuation that still provided sufficient electrical conductivity to sustain an applied voltage. This turned out to be ND 0.2, which corresponds to around 63% transmission.

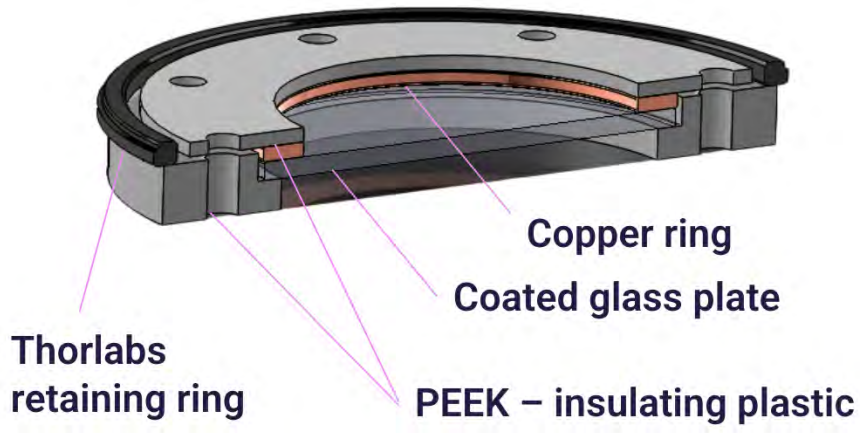

Figure 2.8: Cross-sectional drawing of electric field plate mount.

To supply a voltage to the electric field plates, we clamp a copper ring attached to an external voltage supply to the ND filter's conductive surface (Figure 2.8. We surround these high voltage components with PEEK, an insulating plastic often used in vacuum systems due to its low outgassing rates. We designed our PEEK pieces to be concentric with the ND filter and copper ring, with a roughly 3 inch outer diameter for mounting in ThorLabs 3-inch lens tubes, which are suitable for our application with just a quick addition of holes for the detection laser and molecular beam to travel through. Deploying ThorLabs lens tubes is

convenient not only because they are readily available, but also because they provide a high degree of adjustability. By changing the position of the retaining rings in the lens tube, we can adjust the position of our electric field plates and fine-tune the separation between them, which is a key factor in determining the resulting electric field strength.

(a) Photograph of the electric field plate collection optics assembly

(b) Drawing of the electric field plate collection optics assembly.

The collection optics used to direct laser-induced fluorescence to the detection systems include a condenser lens that collimates light emitted above the molecular beam, a focusing lens positioned above the condenser lens that focuses the collimated light onto the detection tools, and a concave mirror located below the molecular beam that reflects downward-propagating fluorescence back into the optical path toward the same detection system. We mounted each of these components in 2-inch diameter ThorLabs lens tubes, using adapters to interface with the 3-inch tubes used to hold the electric field plates. As with the electric field plates, the use of these lens tubes adds an additional degree of adjustability, allowing us to fine-tune and optimize the positioning of the optics. We install the assembly in our vacuum chamber using an aluminum adapting ring secured to the chamber ceiling, with an inner diameter machined with threads compatible with Thorlabs lens tubes.

2.7 DyO

As the first scientific application, our laser spectroscopy apparatus has been used to characterize the hyperfine structure of dysprosium monoxide (DyO). The electric dipole moment of DyO has previously been measured, making it a convenient molecule with which to calibrate and test our new electric field plates [22]. However, DyO is also an interesting species in its own right and has therefore been the focus of some of our recent spectroscopic studies.

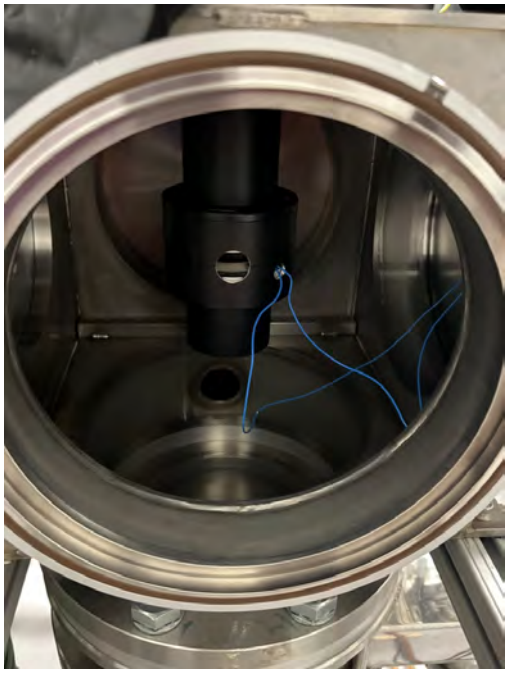

Figure 2.10: Photograph of electric field plate collection optics assembly installed in the vacuum chamber.

DyO has recently been identified as amenable to optical cycling, making it a strong candidate for precision measurements [23]. DyO also displays enhanced sensitivity to BSM physics in the search for the Nuclear Schiff Moment [18]. According to Schiff's theorem, nuclear electric dipole moments are not observable in neutral atoms and molecules because the surrounding electrons will rearrange so as to almost perfectly obscure their effects. This behavior is called screening. However, real atomic nuclei are not point charges and have a spatial extent, so electric fields exist inside them. The Nuclear Schiff Moment (NSM) quantifies the separation in the center of mass and center of charge in an atomic nucleus [24, 25].

Molecules, in many ways, are a more effective platform than atoms for probing symmetry-violating electromagnetic moments such as the NSM. Atomic systems are often constrained by the fact that their atomic orbitals are not fully polarized [18]. In contrast, the electric field required to polarize molecules is small (in particular for polar molecules) and attainable in a lab setting, allowing molecules to become polarized and experience strong internal electric fields [25, 26]. An additional enhancement factor that makes DyO particularly well-suited for precision measurements of fundamental symmetries is dysprosium's octupole-deformed nucleus [24]. The nucleus' asymmetric "pear" shape enhances the internal charge separation, leading to greater effects.

Dysprosium has four isotopes with significant natural abundance: ^{161}Dy, ^{162}Dy, ^{163}Dy, and ^{164}Dy. The odd isotopes have nuclear spin I= 5/2 and the even isotopes have nuclear spin I = 0. For molecules containing heavy atoms such as DyO, excited states are described by the first three digits of the excited state wavenumber relative to the ground state. For instance, the [17.1]7 state of DyO is 17,100 wavenumbers in cm^{-1} above the ground state. The number 7 appearing after the [17.1] indicates the total electronic angular momentum Ω = 7, which sets the lower limit for the rotational quantum number J = 8 at the state. The

rotational energy levels in any molecule are given by

$$E_J = BJ(J+1)$$

where the rotational constant B is related to the molecule's moment of inertia. These rotational levels can split into hyperfine energy levels defined by the hyperfine quantum number F, which goes from J-I to J+I in steps of 1. Since the even isotopes of Dy have 0 nuclear spin and all oxygen isotopes similarly have 0 nuclear spin, species of DyO containing even Dy isotopes do not display hyperfine splitting. P, Q and R branches can be introduced to classify electronic transitions based on differences in the rotational energy levels of the ground and excited state. P denotes ΔJ = -1, Q denotes ΔJ = 0, and R denotes ΔJ = 1. An additional number in parentheses after the letter indicates the initial J state. In the presence of an electric field, each rotational energy level will be split into 2J + 1 sublevels: these will be quantized orientations of the total angular momentum described by quantum number M_J, which takes on values from J to -J in integer steps. Allowed transitions between M_J states vary depending on the polarization of incident light. Light polarized parallel to the electric field will drive $\Delta M_J = 0$ transitions, while light polarized perpendicular to the electric field will drive $\Delta M_J = \pm 1$ transitions [22].

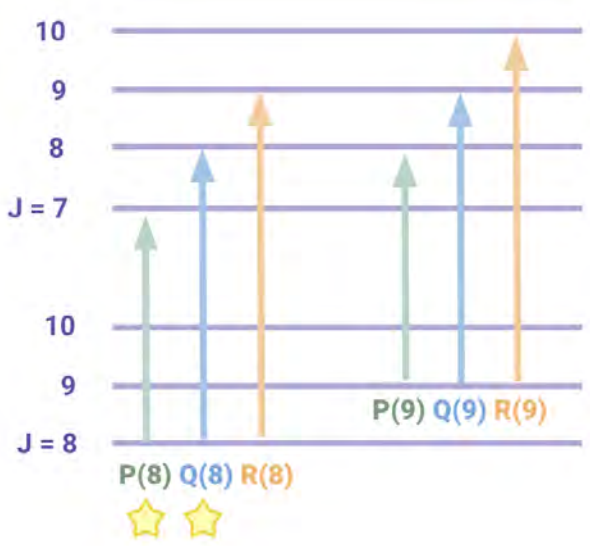

Figure 2.11: Diagram of P, Q, and R transitions from the J = 8 and J = 9 ground states. Transitions using for testing electric field plates — P(8) and Q(8) — are marked with stars.

In collaboration with Zack Lasner (Harvard University), we used our molecular spectroscopy apparatus to determine the hyperfine structure of the ground X8 and excited [17.1]7 states in ^{161}Dy and ^{163}Dy. Incorporating 194 observed transitions from hyperfine-resolved spectra in the (0,0) and (0,1) vibronic bands, we estimated both the magnetic and electric

hyperfine parameters, h and eQq0. These measurements enable implementation of optical cycling and development of precision measurement schemes in addition to benchmarking calculations of the molecule's sensitivity to symmetry-violating effects [18].

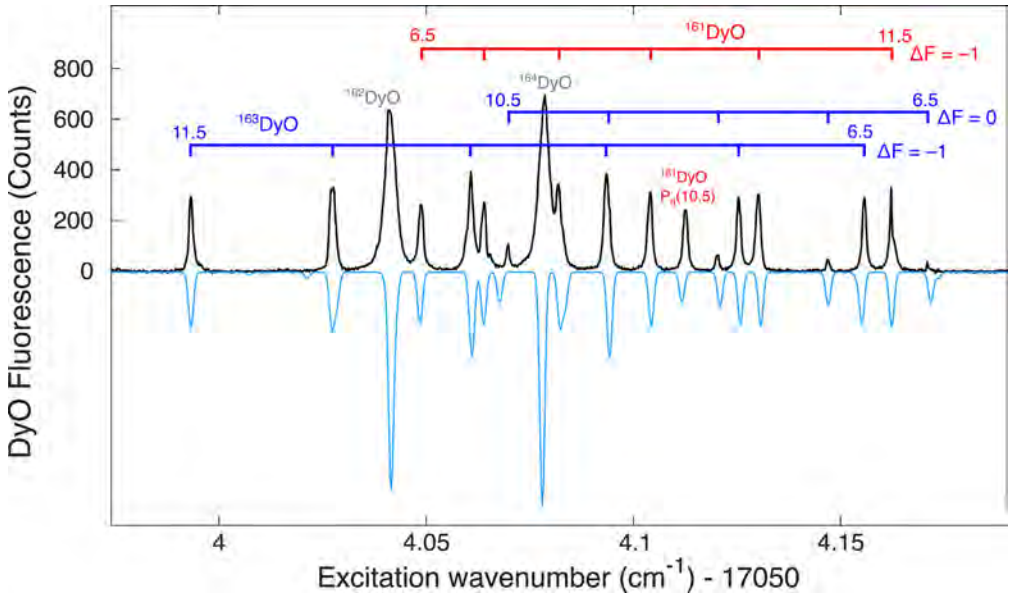

Figure 2.12: Hyperfine-Resolved DyO Fluorescence Spectrum. Observed (black) and simulated (blue) spectra of the [17.1]7 ← X8 (0,0) P(9) branch features are displayed. Simulated spectra were produced using PGOPHER. Figure extracted from [18].

2.8 Testing the Electric Field Plates with DyO

For our initial tests of the electric field plates, we first confirmed that the collection optics were properly spaced by locking our CW dye laser to the [17.1]7 ← X8 (0,1) transition around 616 nm and searching for a signal from ^{162}DyO without turning on the electric field (Figure 2.13). We employed off-diagonal detection, measuring decay at 586 nm to reduce background from detection laser scatter. To isolate this wavelength, we employed a 586 nm bandpass filter above the collection optics assembly in the path to the PMT. We also installed a PBS as the last optic before the vacuum chamber to send perpendicularly polarized light to the molecules.

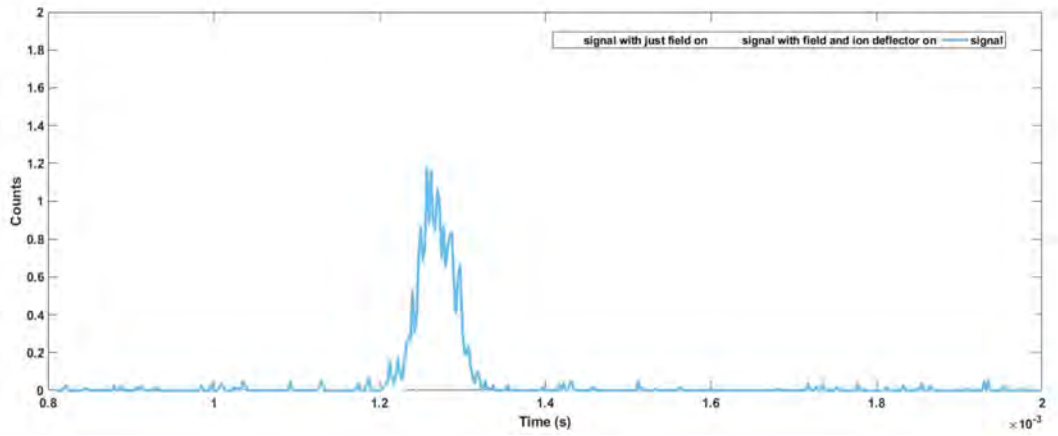

Figure 2.13: Singular time trace for DyO peak detected with new collection optics assembly.

Finding success, we continued our tests by applying a voltage to the electric field plates. When we did this, we observed a large amount of noise that seemed to increase when more voltage was applied. When a voltage of 1 kV was applied, the noise was significant enough to obscure the signal completely (Figure 2.14).

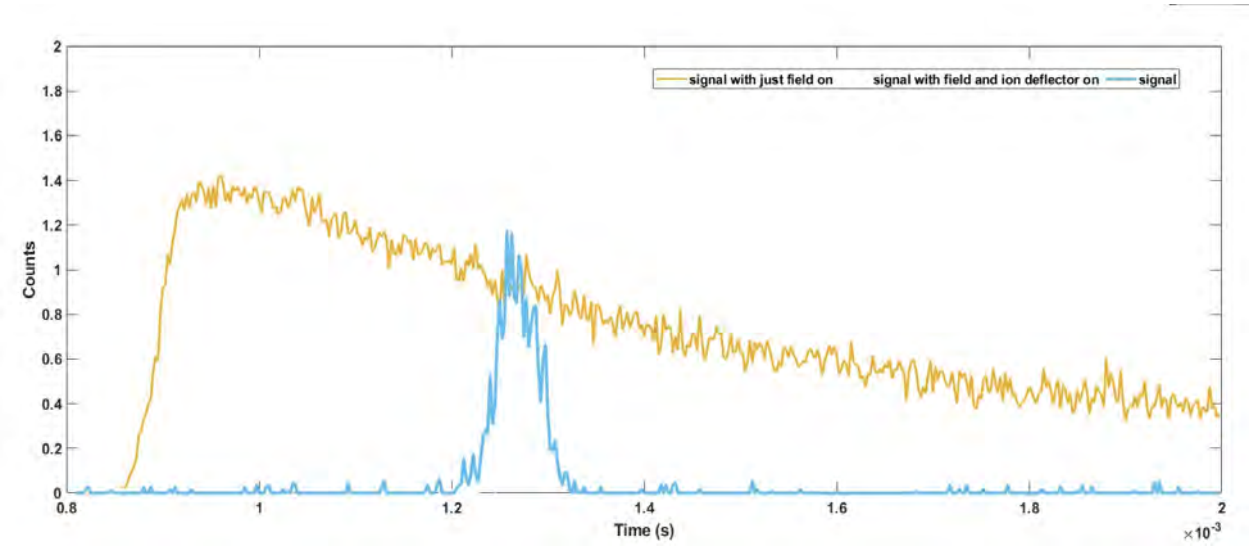

Figure 2.14: Comparison of DyO time trace with and without voltage applied to electric field plates. A voltage difference of 1kV was applied.

We hypothesized that the source of this noise may be due to Bremsstrahlung radiation — lost kinetic energy emitted as electromagnetic radiation when ions present in our molecular beam collide with our electric field plates and are slowed. To eliminate this issue, we installed an additional pair of electric field plates in the molecular beam upstream of the detection site to deflect any ions present in the beam. We calculated the field strength required to

cause the heaviest ions to collide with electric field plates of different length and separation. We did our calculations for the heaviest ions in the molecular beam, which we estimated to be around 200 amu for Au^+ a likely byproduct of AuC production. We estimated the ions in the beam to be traveling at around 600 meters per second. Models based on simple kinematic equations revealed that weak electric fields of a few V/cm are sufficient.

The addition of these ion deflector plates eliminated the noise we had observed previously, and allowed us to detect Stark-shifted spectra in DyO. We examined the Q(8) branch first, since its structure is simpler. For incident light polarized perpendicular to the electric field, since both the ground and excited state split into 8 sub-levels, there are 16 $\Delta M_J = 1$ and 16 $\Delta M_J = -1$ transitions. These are sorted into two unresolved groups symmetrical about their position with zero field applied [22].

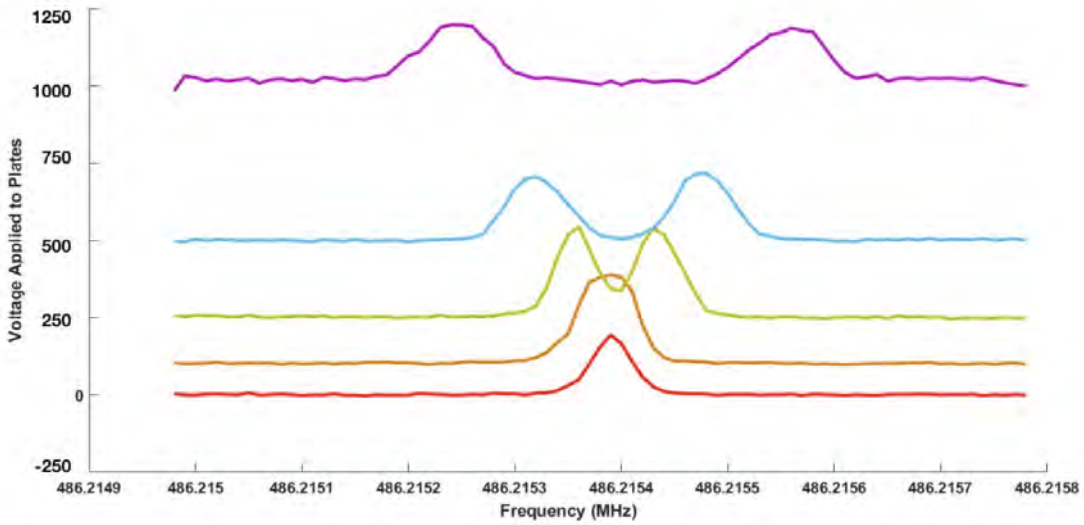

Figure 2.15: Stark effect in the Q(8) line of the 0-1 band of the [17.1]7 $\leftarrow$ X8 transition of DyO. As the voltage applied to the electric field plates increases, the Stark effect also increases.

Then, we interrogated the P(8) branch near 486.083 THz, where we expect to see a more complex pattern with 7 peaks instead of 2 peaks. For the P(8) branch, the ground state has 17 sub-levels while the excited state has 15. In this case, we would expect 15 $\Delta M_J = 1$ and 15 $\Delta M_J = -1$ for a total of 30 transitions. However, exact coincidences of $\Delta M_J = 1$ and $\Delta M_J = -1$ yield seven intense lines in the center[22].

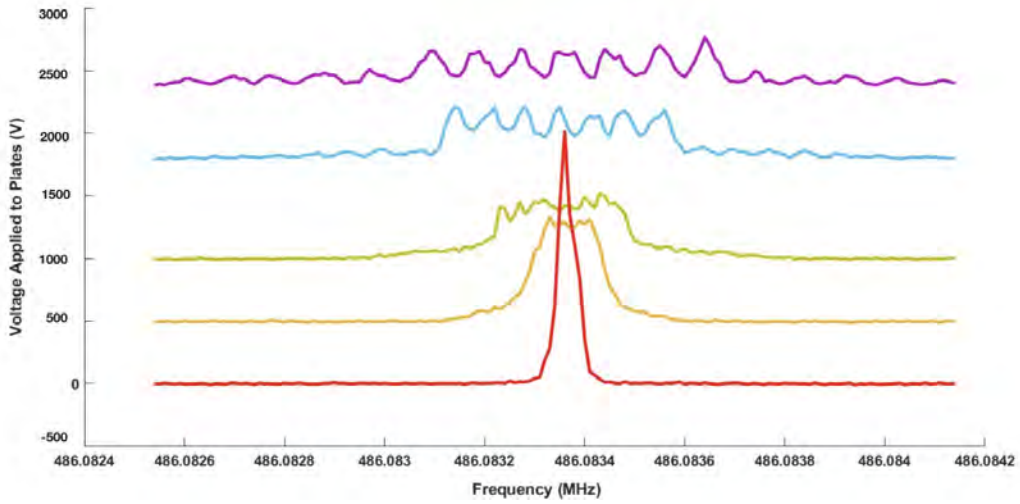

Figure 2.16: Stark effect in the P(8) line of the 0-1 band of the [17.1]7 ← X8 transition of DyO

When we are running the experiment, the sole parameter we have control over is the voltage difference we choose to apply to the electric field plates. Given the geometry of our plates, we have an estimate of what electric field an applied voltage difference corresponds to, but there are complications that may arise from factors including that the plates are finite, the spacing between the plates is not known precisely, there are other materials around, and edge and fringing effects may exist. DyO's permanent dipole moment has been well-characterized (¡ 1% relative standard deviation), so we were able to use our Stark-shifted spectra to "calibrate" our electric field plates, obtaining a more precise measure of our applied electric field.

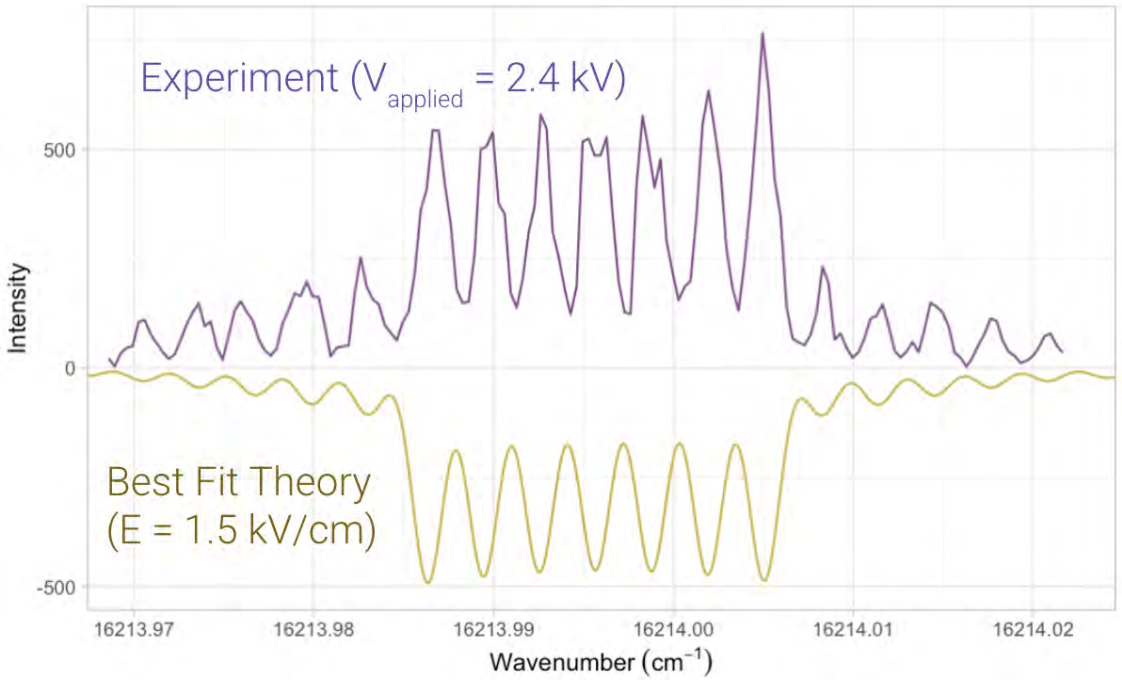

Figure 2.17: Stark effect in the P(8) line of the 0-1 band of the [17.1]7 -X8 transition of DyO when 2500 V were applied to the electric field plates. The simulated peaks are derived from PGOPHER under an electric field strength of 1500 V/cm.

In our PGOPHER simulations, the closest match we found to our most Stark-shifted spectrum (2400 V applied) came from an electric field strength of 1500 V/cm. In a first-order approximation, the electric field strength depends on the voltage applied to the capacitor plates and the separation between the plates. If we model our plates as infinite parallel plate capacitors, the electric field between them should be equal to a ratio of the voltage difference and separation distance $E = \frac{V}{d}$. The electric field should approximately be equal to a ratio of the voltage difference and separation difference $E = \frac{V}{d}$. Based on our electric field of 1500 V/cm and voltage difference of 2400 V, we estimate that our plates are 1.6 cm apart, which seems reasonable. Between the knowledge of DyO and the quality of this comparison, we are confident about the magnitude of the electric field that we are producing to a few %, which is sufficient for the accuracy of our future experiments.

Chapter 3

Frequency-Doubled Laser Source for Lead Cooling

High-precision spectroscopy of lead, one of the heaviest known stable elements, has been the recent focus of experimental efforts in the Majumder Lab. In the 1990s, measurements of parity non-conserving optical rotation were performed on atomic lead [27, 28]. Cooling of the lead atomic beam in the Majumder Lab may enable detection of the 462 nm M1 transition, a weak and therefore elusive transition, but one that is promising for a new atomic parity non-conservation experiment. Four stable isotopes of lead exist in nature: ^{204}Pb, ^{206}Pb, ^{207}Pb and ^{208}Pb. Laser-cooled and trapped samples of lead atoms have the additional potential to yield new precision measurements of differences in atomic parity non-conservation across these isotopes.

Lead-containing diatomic molecule species such as AgPb and AuPb have also been proposed as viable candidates for electron EDM searches [19], making them of interest to the Augenbraun Lab. These diatomic molecules can be assembled from separately laser-cooled atomic samples of the coinage metal and lead. Ag has been successfully laser-cooled, and a similar scheme to demonstrate laser-cooling in Au has been proposed. Therefore, a first demonstration of laser-cooling in lead would mark a significant milestone towards producing these species.

The ability to laser cool lead is a pre-cursor to improving both experimental efforts and may be key to probing physics beyond the Standard Model. Thus, the Majumder Lab and Augenbraun Lab are collaborating to demonstrate laser cooling in lead.

3.1 Experimental Plan

Accomplishing our goal of demonstrating laser cooling in lead atoms requires (1) creating an atomic beam source for lead, (2) cooling the lead atoms using laser light, and (3) imaging the beam afterwards to verify that cooling has occurred.

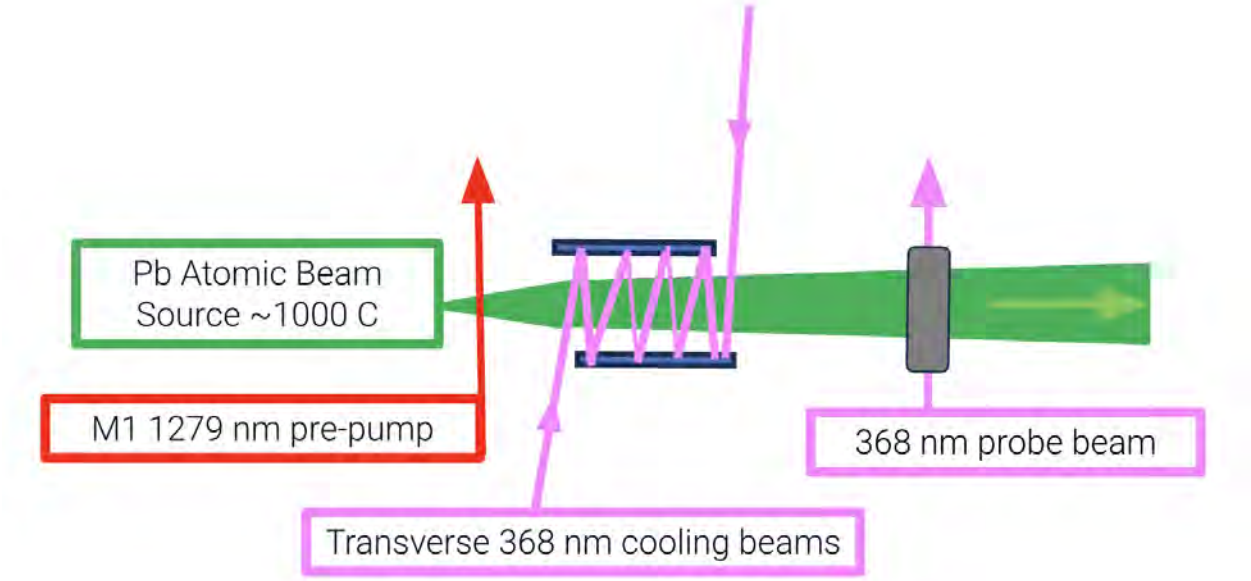

Figure 3.1: Sketch of transverse laser-cooling scheme, overhead view.

3.1.1 Atomic Beam Source

The atomic beam apparatus in the Majumder Lab, previously used for indium and thallium polarizability measurements, has been upgraded and repurposed for lead (Figure 3.2). Our existing vacuum chamber has two regions, a source region and a science region. The atomic beam source, discussed in further detail in previous theses and publications [29, 30], resides in the source region and features a cylindrical Molybdenum crucible containing around 200 g of lead (Figure 3.3. The crucible is enclosed in a cylindrical tube, which is in contact with two semi-cylindrical tubes held at high temperatures through resistive heating. The heating system is insulated by two layers of carbon fiber felt with a stainless steel tube in between. A water-cooled copper shield provides the final layer of defense after the insulation to prevent heat from radiating into the science chamber. The heating system can operate up to 1050 °C. We monitor the temperature inside our chamber with four thermocouples that are attached to the crucible, the heater, the stainless-steel heat shield, and the water-cooled copper wall.

The crucible is capped by a face plate with a thin slit pattern, which helps decrease the divergence of the beam and reduce Doppler broadening. As the atoms exit the crucible and travel toward the science chamber, the beam is further collimated using two razor blades. We plan to demonstrate one-dimensional (transverse) cooling of our atomic beam in the science chamber. Cooling the beam in the transverse direction would result in an even more collimated beam and consequently even less Doppler broadening [31].

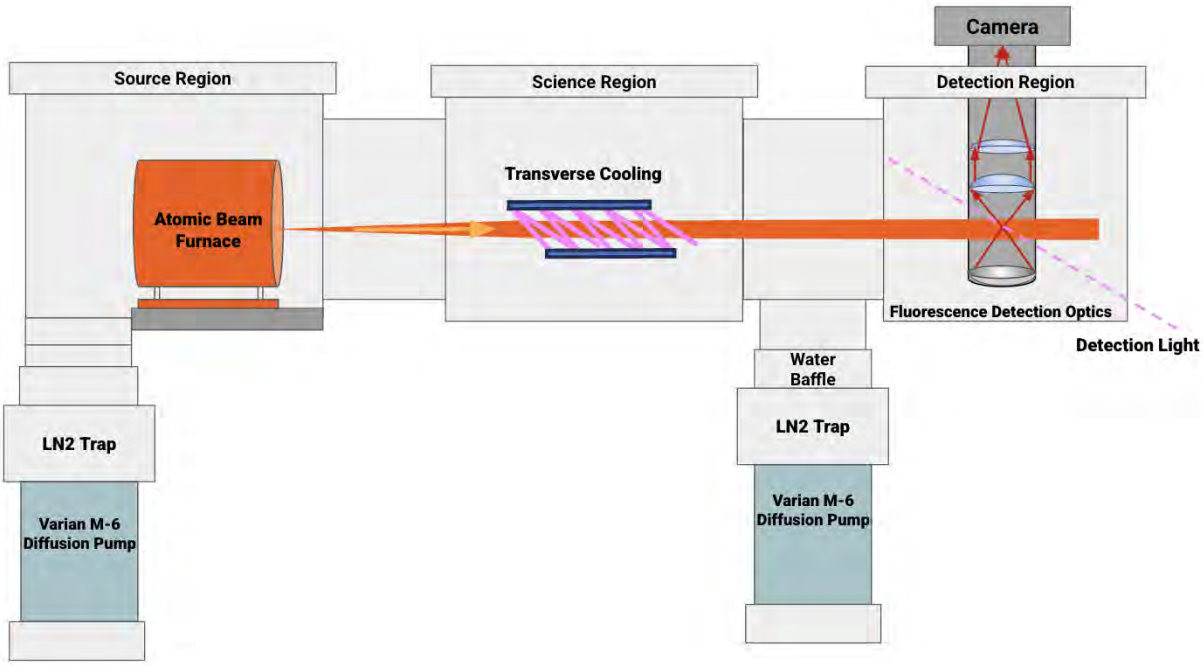

Figure 3.2: Diagram of vacuum chamber and atomic beam apparatus, modeled after Figure 4.1 in [29]. Designs for the addition of the detection region are underway.

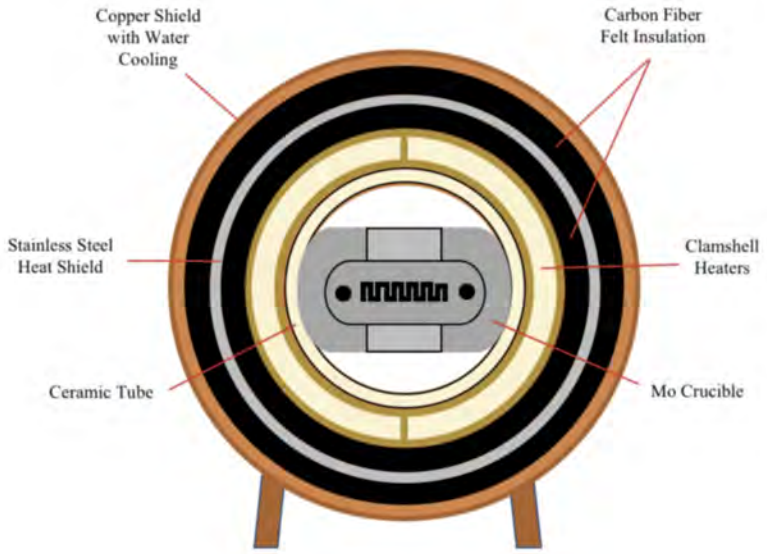

Figure 3.3: Front-view diagram of the heating system for the Molybdenum crucible. Figure repurposed from [29].

3.1.2 Laser Cooling Lead

Previous work in the Majumder Lab has characterized the amplitude and polarizability of the 368 nm electric-dipole (E1) transition from the $6s^2 6p^2\ ^3P_1$ state to the $6s^2 6p7s\ ^3P_0$ state in Pb-208 (Figure 3.4 [32]. The E1 transition is able to support optical cycling since once excited to the $^3P_0$ state, atoms can only decay to the original $^3P_1$. ΔJ between transitions is only allowed to take on values of 0, +1, and -1. Transitions from J=0 to J=0 are forbidden, which means that the J = 0 $^3P_0$ excited state can only decay to the J = 1 $^3P_1$ ground state since there is no state with J = -1. Furthermore, the excited state lifetime of the $^3P_0$ state (5.7 ns) is relatively short, enabling a high photon scattering rate of 175 MHz.

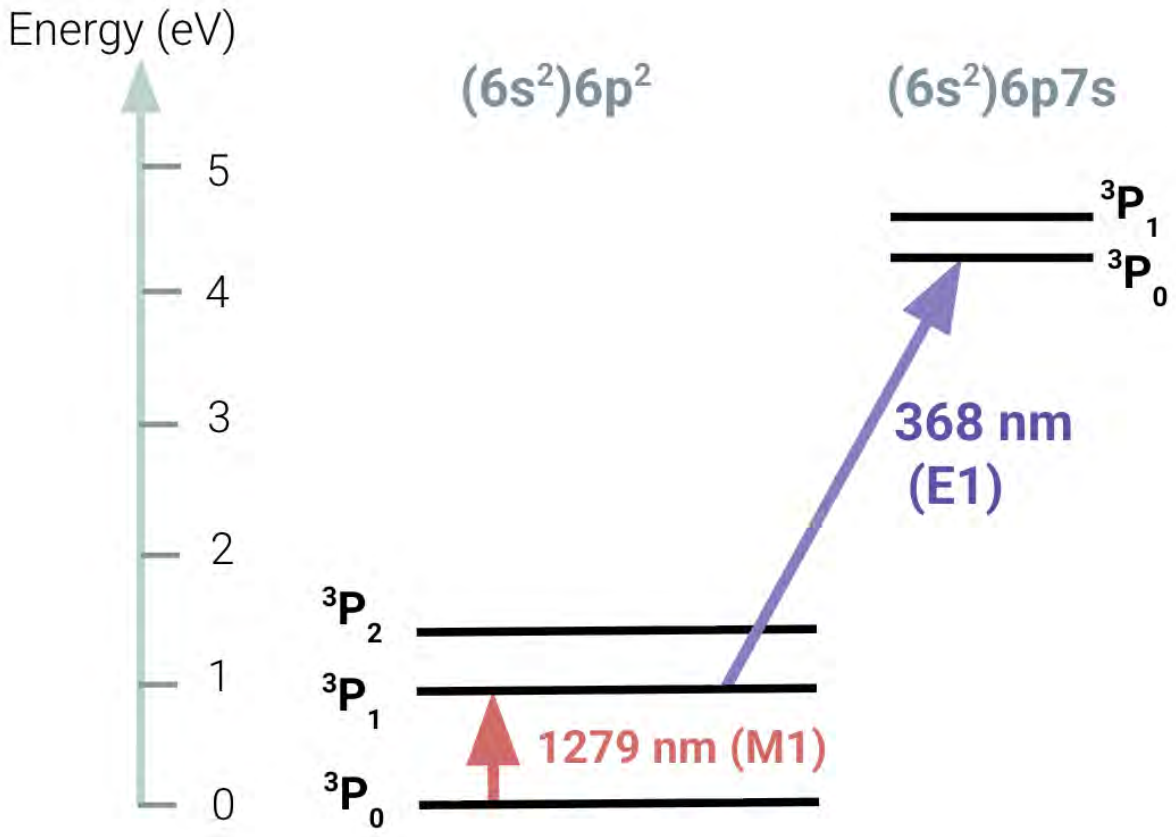

Figure 3.4: Selected low-lying energy levels of Pb-208. Relevant transitions, including the 368 nm optical cycling transition, are highlighted.

The 368 nm transition does not originate from the ground state, but rather from the $^3P_1$ state. The relative thermal population of the two states can be estimated using the Boltzmann factor, which approximates the ratio of excited atoms to ground-state atoms as $e^{-\Delta E/kT}$. At 1000 °C, the rough temperature of our atomic beam source, the thermal population in the $^3P_1$ state is around 10^{-4} times the thermal population in the ground state.

We can enhance the excited state population using 1279 nm laser light to drive the M1 transition from the ground state. Since the M1 transition is forbidden and weak, the $^3P_1$ state is a metastable state and has a long natural lifetime of around 250 ms. Because there are minimal collisions in the low-density atomic beam, this long lifetime prior to spontaneous decay allows atoms to remain in the $^3P_1$ state once optically pumped. We have verified this enhancement of excited state population in a lead vapor cell, identifying an increase in the size of the 368 nm E1 signal when 1279 nm optical pumping was implemented [33].

There is a possibility of atoms in our beam becoming trapped in magnetic dark states where they can no longer respond to the light field after interacting with the cooling light [34]. This would be detrimental because atoms in dark states cannot be optically cycled for cooling. The dark states are Zeeman sub-levels of the lower energy state in our optical cycling pathway. To avoid accumulating atoms in these dark states, we plan to install a magnetic field oriented at a 45°angle with respect to the atomic and laser beams to induce Larmor precession. The ensuing mixing of the Zeeman sub-levels allows atoms in the dark states to cycle out of the dark states and be re-coupled to the light field [35].

As depicted in Figure 4.1, we plan to first enhance the excited state population using 1279 nm light. Then, we will use optical fibers to launch counter-propagating 368 nm laser beams in the transverse direction. Parallel mirrors will direct the cooling beams to make multiple passes through the cooling region of the atomic beam. A magnetic field will be present in the cooling region to prevent dark-state accumulation.

Achieving cooling requires laser light at 1279 nm and 368 nm. Not only do we require lasers capable of generating light at these wavelengths, we need reliable methods of stabilizing the lasers at each wavelength. From our previous lead experiments, we have an external cavity diode laser (ECDL) system purchased from Sacher Lasertechnik capable of producing 1279 nm light. Julia Matin '25.5 developed a locking scheme for this laser system using a function generator, a PID controller, and a lock-in amplifier.

We modeled Doppler cooling in our atomic beam in a Monte Carlo simulation, assuming optimal red de-tuning in our cooling beams, a 5-10 K average transverse temperature before cooling, and a source temperature of 1000 C alongside other atomic beam parameters. Based on our results, we predict that at least 100 mW of UV light will be required to observe 25% narrowing of our beam in the downstream detection region. Our lab has a home-built ECDL laser at 368 nm [29]. This ECDL system can be locked on the E1 transition and implemented in fluorescence detection to image the beam downstream of the cooling region, a process discussed in the next sub-section. However, the current system cannot generate the 100 mW required for the cooling beams. We have designed a new laser system for this cooling application using a frequency-doubled CW Titanium-sapphire (Ti:Sapph) laser which operates in the infrared.

3.1.3 Imaging the Beam

We intend to expand our vacuum chamber and add a downstream detection region where we will image the atomic beam through fluorescence detection after it has been laser cooled.

The principle of operation for fluorescence detection is similar to that for the fluorescence spectroscopy described in Chapters 2 and 3. Laser light from our existing 368 nm ECDL system locked to the E1 transition will excite atoms in the beam to the $^3P_0$ state. As the atoms spontaneously decay down to the $^3P_1$ state, optics will collect and focus the fluorescence to be imaged on a camera. In addition to the UV light, which will be single-passed through the atomic beam, we will also introduce magnetic fields to prevent dark-state accumulation at our detection site. Not only must our imaging system achieve sufficient overall photon detection rates, it must possess sufficient spatial resolution to detect small changes in the atomic beam profile due to laser cooling.

Other students in the group have taken on the task of designing and integrating these upgrades for the vacuum chamber. Assembling the new laser system necessary for laser cooling is the primary goal of the work described in this chapter.

3.2 Laser System

As previously mentioned, we have designed a new laser system to produce the high power ultraviolet light for laser-cooling. Dan McCarron (UConn) has kindly loaned the Augenbraun Lab a Coherent 899 Ti:Sapph laser capable of producing 0.5 - 1 W of laser light at 736 nm, twice our wavelength of interest. We can double the frequency from this laser, achieving our desired wavelength of 368 nm by implementing a non-linear crystal that produces second harmonic light. By placing the crystal in a bow-tie cavity, we can enhance the output power.

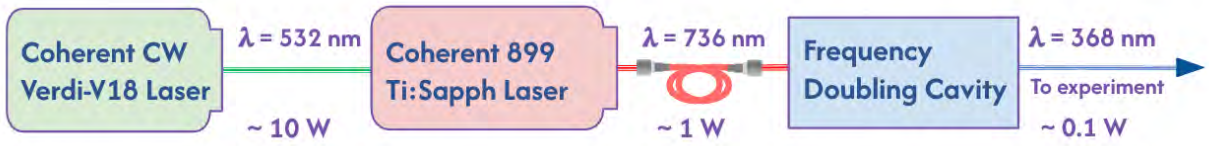

Figure 3.5: Schematic overview of the proposed 368 nm laser system. Pumped by 532 nm light, a titanium-sapphire (Ti:Sapph) laser produces 0.5-1 W of light at 736 nm. The 736 nm light then enters a doubling cavity, becoming 368 nm light with the help of a nonlinear crystal.

3.2.1 Nonlinear Optics

We must frequency double the light produced by the Ti:Sapph in order to obtain the 368 nm light that probes our cycling transition. To do this, we take advantage of the unique nonlinear behavior of a lithium triborate (LBO) crystal when exposed to laser light.

Neutral atoms and molecules can become polarized when placed in a sufficiently large electric field, such as that produced by laser light. For instance, an electric field incident

upon a neutral atom will push the positively charged nucleus in the direction of the electric field while pulling the negatively charged electron cloud in the opposite direction, inducing a dipole moment. For neutral dielectric materials (which possess only bound electrons, unlike conductors), the polarization ($\mathbf{P}$), or dipole moment per unit volume, captures the aggregate effect of the induced dipole moments of each individual atom or molecule in the material. The polarization induced by the incident electric field generates an electric field of its own. This additional electric field further modifies the polarization, generating even more components of the electric field.

In linear dielectric materials, the resulting polarization is proportional to the total electric field as long as the field is not too strong.

$$\mathbf{P}(t) = \varepsilon_0 \chi_e \mathbf{E}(t)$$

Crystals are often easier to polarize in some directions than in others, in which case the electric susceptibility χ_e can be replaced by a susceptibility tensor. The permittivity of free space ε_0 in the expression ensures that these proportionality constants can remain dimensionless [8].

Our nonlinear crystal, LBO, falls within a class of materials used in modern optical applications for which the polarization resulting from interactions with an electric field has additional components that are proportional to powers of the electric field. The polarization of these non-linear materials can be modeled as a power series in the electric field strength

$$\mathbf{P}(t) = \varepsilon_0(\chi_e^{(1)}\mathbf{E}(t) + \chi_e^{(2)}\mathbf{E}^2(t) + \chi_e^{(3)}\mathbf{E}^3(t) + ...)$$

where $\chi_e^{(n)}$ represents the n-th order susceptibility tensor. These additional components of the polarization yield new components of the electric field that oscillate at frequencies other than the frequency of the incident field. Therefore, crystals that possess these non-linear properties are implemented in frequency conversion processes—second harmonic generation, sum and difference frequency generation, optical parametric oscillation, and others [36].

3.2.2 Frequency Doubling

During second harmonic generation, a photon of frequency 2ω (the second harmonic frequency) is created in exchange for two incident photons of half that frequency, ω. Crystals like LBO that are suitable for second harmonic generation have non-zero second-order susceptibility tensors. Then, given incident laser light whose electric field strength can be represented by

$$\mathbf{E}(t) = Ee^{-i\omega t} + E^* e^{i\omega t},$$

the second order polarization

$$\mathbf{P}^{(2)}(t) = \epsilon_0 \chi_e^{(2)} \mathbf{E}(t)^2$$

of these crystals contain a zero frequency contribution and a contribution at the second harmonic frequency 2ω:

$$\mathbf{P}^{(2)}(t) = 2\epsilon_0 \chi_e^{(2)} EE^* + (\epsilon_0 \chi_e^{(2)} E^2 e^{-2i\omega t} + \epsilon_0 \chi_e^{(2)} E^2 e^{2i\omega t}).$$

In line with the driven wave equation, terms with frequency 2ω result in electromagnetic radiation at the second harmonic frequency [36].

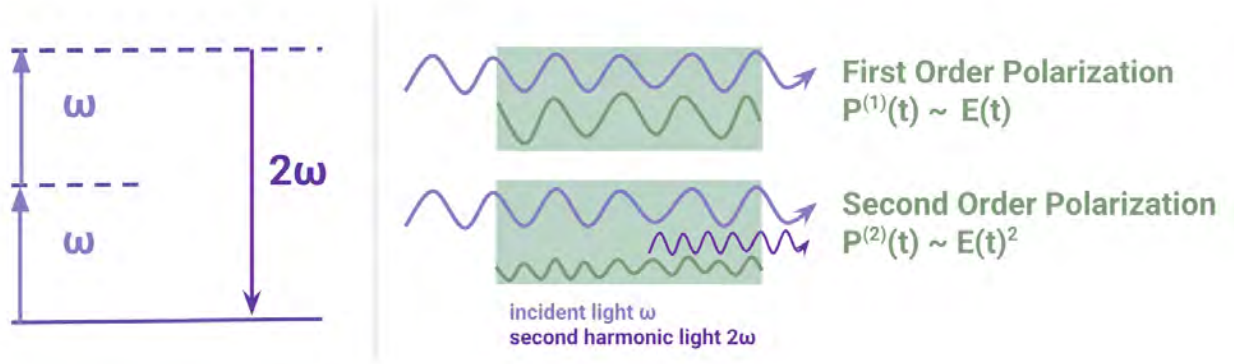

Figure 3.6: Left: Energy-level diagram depicting the production of one 2ω photon from two ω photons during second harmonic generation. Right: Representation of first and second order polarization and corresponding electromagnetic radiation in a nonlinear medium. Second order polarization leads to radiation of second harmonic light. Adapted from *Nonlinear Optics* by R.W. Boyd (Figure 1.2.1).

Efficient second harmonic generation requires a fixed phase relationship between interacting light waves at the crystal's exit face. In the absence of phase matching, destructive interference will reduce the outgoing power. In LBO (and most nonlinear crystals), the index of refraction depends on the polarization of incident light relative to the crystal's axes, so we can achieve phase matching by adjusting the angle of the crystal's axes relative to the orientation of incoming light.

3.2.3 Bow Tie Cavity

The amount of second harmonic light generated in this process pales in comparison to the intensity of fundamental frequency light transmitted through the crystal. Therefore, we use a bow-tie enhancement cavity to amplify and isolate second harmonic light. The Majumder Lab owns a Wavetrain Frequency Doubling Cavity produced by Laser Analytical Systems, last used to produce ultraviolet light to probe the 378 nm transition in atomic thallium in the early 2000s. Refurbishing the cavity after two decades requires replacing the LBO crystal, which has degraded as a result of exposure to humidity over time, in addition to testing the various mirrors and electronics involved. We will conduct these tests first with a new crystal cut for the system's original wavelength (378 nm) before inserting a crystal suited for our desired wavelength (368 nm).

The bow-tie cavity increases the output power at the second harmonic by enhancing the amount of the fundamental frequency light (736 nm) that is incident upon the crystal. Mirrors 1-4, which comprise the "bow-tie," are all highly reflective near 736 nm. Once fundamental frequency light from the Ti:Sapph is set on the correct course by the folding

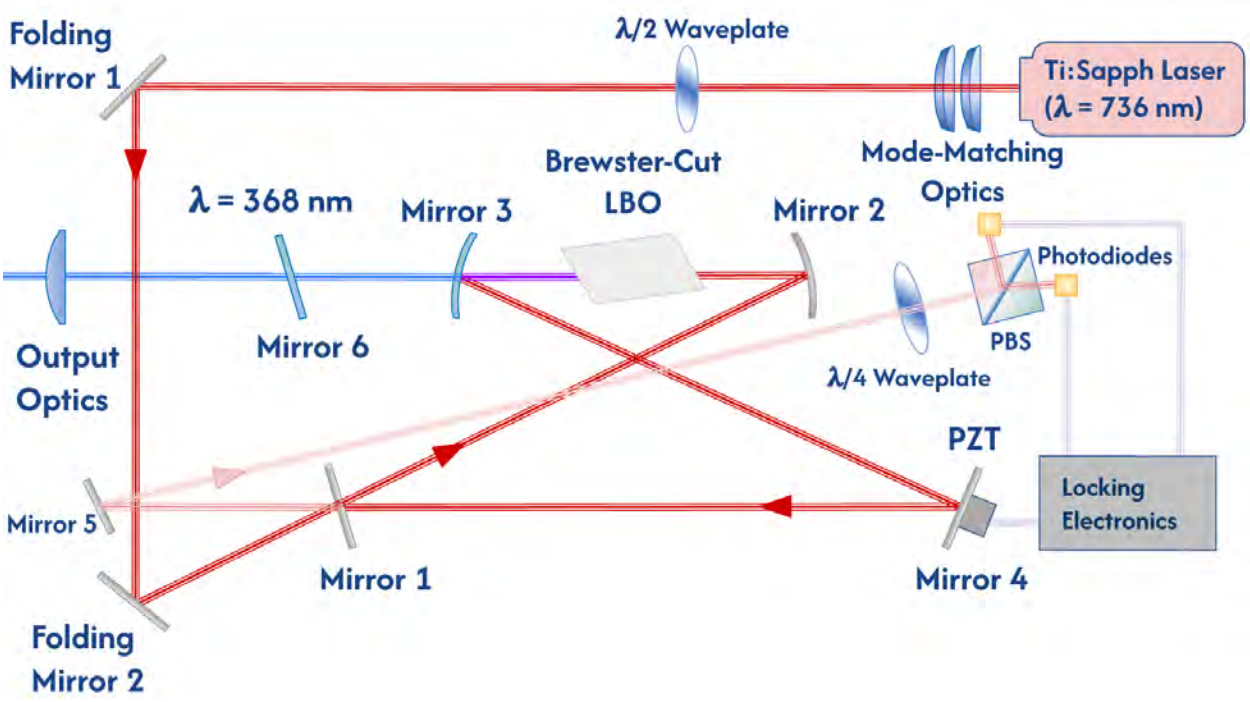

Figure 3.7: Schematic overview of the LAS Wavetrain Frequency Doubling Cavity. Mirrors 1, 2, 3, and 4 comprise a bow-tie enhancement cavity. Mirror 3 allows second harmonic radiation to pass through while reflecting light at the fundamental frequency to continue cycling around the cavity, maximizing second harmonic generation by increasing the amount of 736 nm light incident upon the LBO crystal.

mirrors, the bow-tie arrangement of these four mirrors direct the infrared light to cycle through the crystal many times. In order for the fundamental light to interfere constructively with itself, the cavity must be operating in an eigenmode for the fundamental frequency. This requires that the fundamental frequency light be in the same configuration when it returns to its starting point after each cycle through the four mirrors and nonlinear crystal. During each cycle, the second harmonic light generated exits the bow-tie system through Mirror 3, which is actually a short wave pass dichroic beamsplitter that reflects the fundamental frequency while transmitting the second harmonic frequency. Mirror 6 is also a dichroic that transmits only the second harmonic frequency and not the fundamental. Power loss due to reflection at the nonlinear crystal entry face is minimized by cutting the crystal face such that the beam coincides with the crystal at Brewster's angle, which we calculated for 736 nm to be 57.5 degrees.

We ensure that the cavity is operating in an eigenmode of the fundamental frequency by using a piezoelectric transducer (PZT) to adjust the placement of Mirror 4 and thus tune the path length. The locking system that provides feedback to the PZT relies on the polarization of the beam being uniform. We insert a half-waveplate into the fundamental beam prior to entering the doubling system to ensure the light is vertically polarized when it enters the

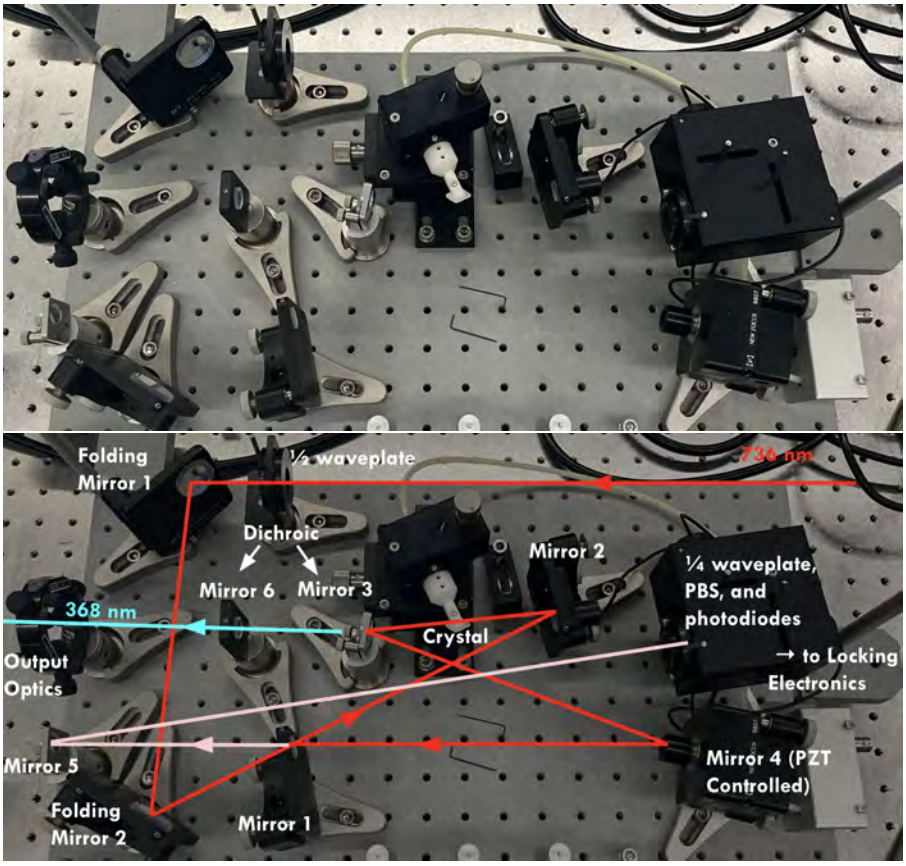

Figure 3.8: Photograph of the LAS Wavetrain Frequency Doubling Cavity.

cavity. At mirror 1, the majority of light enters the bow-tie cavity, but a small portion of the light is reflected off and redirected to Mirror 5. The cavity is the correct length if the light coming back to Mirror 1 after each cycle is in phase with the light reflected and redirected to Mirror 5. Each cycle, a small amount of fundamental light that returns to Mirror 1 is transmitted and directed to Mirror 5 to make this comparison. If the cavity is aligned and operating in an eigenmode, the fundamental frequency beam reflected by Mirror 5 will have the vertical polarization that it did when it entered the cavity. The quarter-waveplate will split the beam into orthogonal linearly polarized beams of equal amplitude, which is then split by the polarizing beamsplitter and read on the photodiodes as equal signals. If the light returning the Mirror 1 is out of phase with the original beam, the beam reflected by Mirror 5 will be elliptically polarized light, so the amplitudes of the resultant linear components will be unequal after the quarter waveplate and the polarizing beam splitter. Their difference is used to determine whether the cavity is long or short, and this information is sent to the PZT to make the necessary adjustments.

3.3 Experimental Progress

We have successfully generated infrared light with our Ti:Sapph laser and demonstrated wavelength stabilization through PID control. We have also ordered a replacement frequency crystal cut for 378 nm.

3.3.1 Ti:Sapph Laser Alignment and Troubleshooting

Capable of continuous tuning from around 700 nm to 1020 nm, the Ti:Sapph is one of the most widely tunable lasers on the market. With 10-15 W of pump light at 532 nm, Ti:Sapph lasers can achieve high output (over 1 W) and narrow-band radiation across most of their spectrum. The Coherent 899 ring laser body can be used as a continuous wave dye laser or a Ti:Sapph laser. The optical layout for the laser in Ti:Sapph form is depicted in Figure 3.9. Three "periscopes" P1, P2, and P3 work in conjunction with lens L1 to direct and focus the 532 nm pump beam through the Ti:Sapph crystal. The majority of pump light is transmitted through mirror M5 and deposited on a beam dump after a pass through the crystal.

The cavity of the Coherent 899 laser consists of four mirrors, the Ti:Sapph crystal, an optical diode, a birefringent filter, a Brewster plate, and a thick and a thin etalon (housed in the intracavity assembly or ICA). The laser has a tendency to operate in both directions, which is a problem because it can lead to spatial hole burning from standing waves. The optical diode applies the Faraday effect to prevent this and ensure that the laser operates uni-directionally. The birefringent filter provides coarse frequency control. For fine frequency control, the piezo-electric (PZT) driven mirror often known as the "tweeter" can be used to change the cavity length at a rapid frequency. The scanning Brewster plate also changes the path length by rotating, but it does so at a slower rate. A pair of etalons, low finesse Fabry-Perot filters, in the ICA add additional stability. The thin etalon acts as a "tracking filter," providing a rigid reference for locking the laser wavelength. After the laser light exits the cavity through the output coupler M4, a small amount is picked off and sent to built-in external reference cavity that the laser can be stabilized with [37].

The laser can be difficult to align, but we found success following the instructions in the operator's manual for operation in single frequency with a high power pump. Further alignment suggestions are provided in Appendix C.2. After spending many hours fiddling, we were overjoyed to achieve multi-mode oscillation without the installation of the ICA or the Brewster plate. At this stage, we expected to be producing around 1 W of light with around 12 W of pump power. However, even after re-starting the alignment process multiple times and optimizing alignment to maximize output power each time, the highest amount of output power we observed was around 750 mW. We investigated the behavior of the laser, making rough frequency adjustments by rotating the birefringent filter and taking measurements of the output power as a function of wavelength (Figure 3.11).

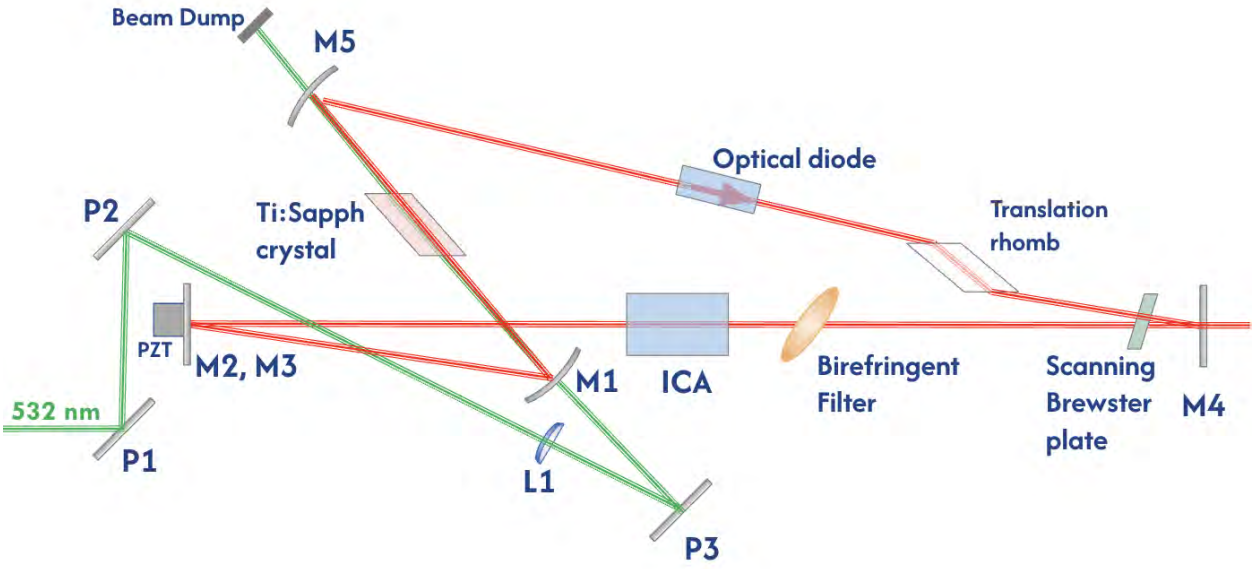

Figure 3.9: Optical Layout of the Coherent 899 Ti:Sapph Ring Laser.

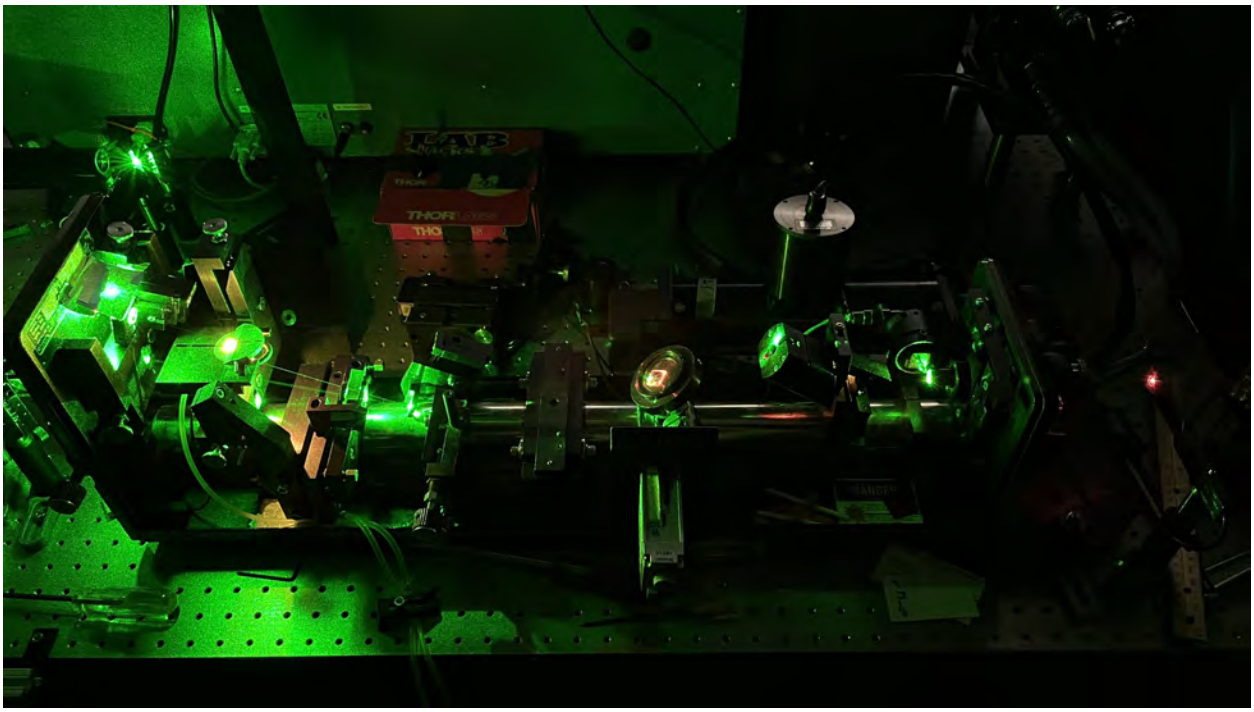

Figure 3.10: Photograph of our Coherent 899 Ti:Sapph Ring Laser in operation, prior to installing the intracavity assembly (ICA) and scanning Brewster plate.

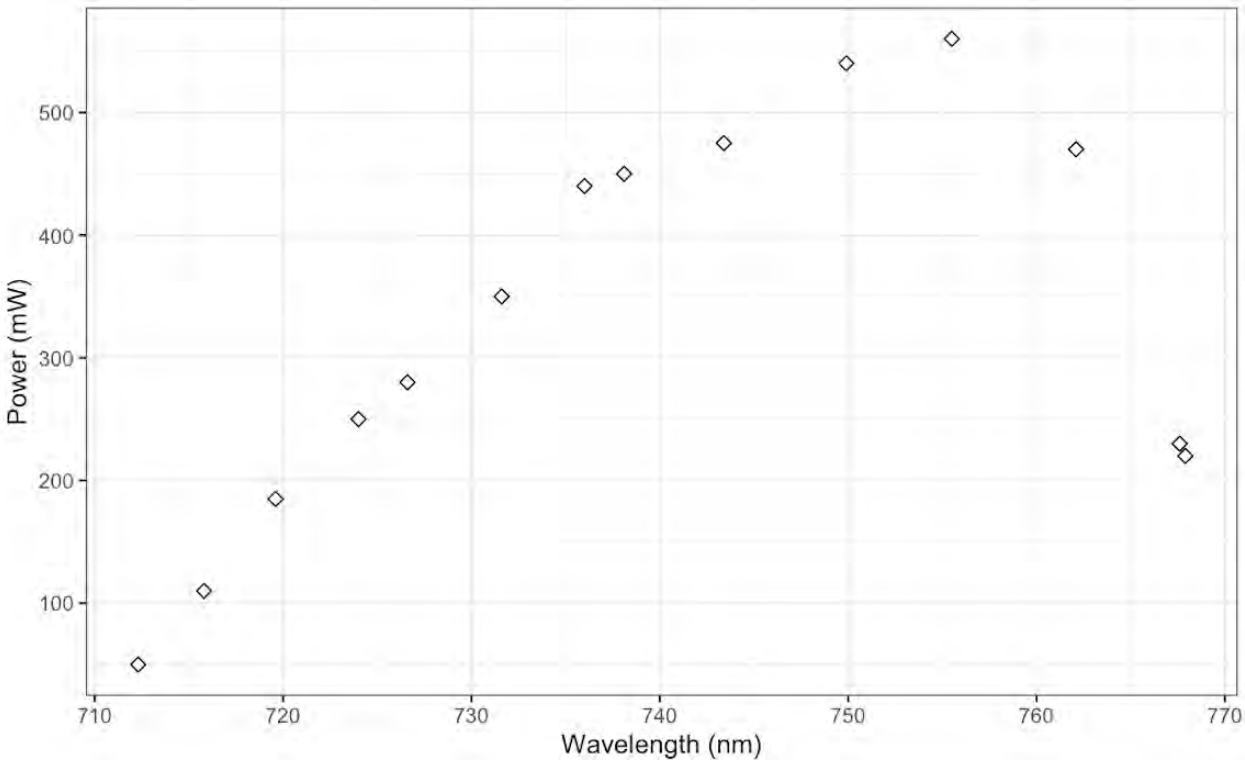

Figure 3.11: Ti:Sapph laser output power as a function of wavelength after initial alignment.

Notably, we observed a steep decrease in output power once the wavelength became longer than 755 nm. This was cause for concern because the Ti:Sapph should be capable of producing wavelengths well into the 800 nm range. The laser's inability to tune within the infrared region made us suspicious of the proper functioning of our optics. To investigate our suspicions, we began by removing the most easily accessible mirrors, M1 and M5, from the laser cavity and examining their performance using 780 nm laser light from an ECDL laser system. M1 is the lower fold mirror and M5 is the upper fold mirror. Since both serve as cavity mirrors and neither act as the output coupler, both mirrors must be highly reflective. We measured the reflectance of each mirror $R = \frac{P_r}{P_i}$ for various angles of incidence, reading the power of the incident (P_i) and reflected (P_r) laser light from a powermeter (Figure 3.12).

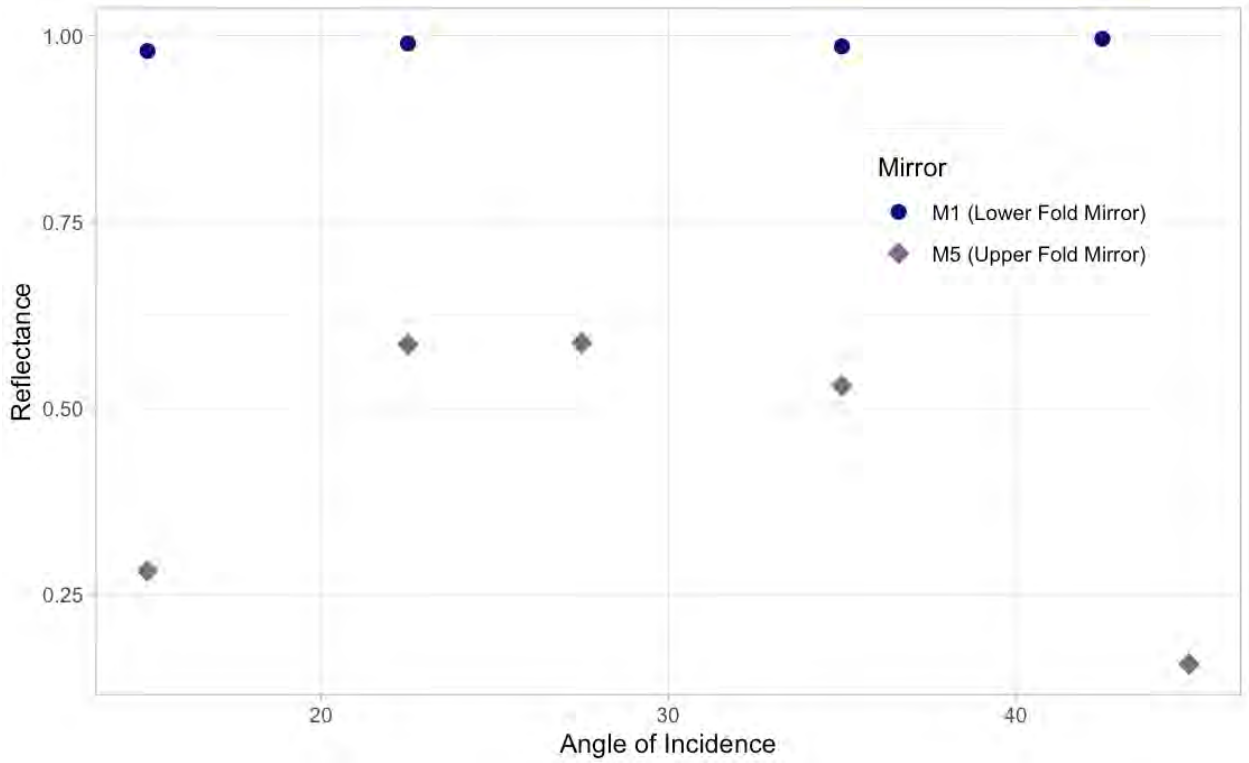

Figure 3.12: Measured reflectance of Ti:Sapph lower fold mirror M1 and upper fold mirror M5 at 780 nm. All angles of incidences are approximate.

By making these measurements, we discovered that the upper fold mirror (M5) we were using was not in fact a Ti:Sapph mirror, but instead one coated for the visible range left over from when the Coherent 899 was used as a dye laser. We calculated reflectances close to unity as expected for the lower fold mirror (M1), which assured us that our method of measuring reflectance was effective. Using the same method, we found that the M5 mirror's reflectance peaked at only 0.58 at 780 nm, explaining our laser's rapid performance decline for wavelengths surpassing 755 nm.

Fortunately, we had a spare mirror in the lab and were able to immediately replace the faulty M5 mirror. Not only did replacing the mirror lead to greater tunability across the infrared region, aligning and achieving laser operation became much easier. With the new mirror, we were able to generate 850 mW of light at this intermediate step in the alignment process, prior to adding the ICA and Brewster plate. We estimate a retention of around 60% of this output power after inserting the ICA and scanning Brewster plate. To date, we have seen a maximum of roughly 400 mW of single-frequency radiation with those two optics installed.

3.3.2 Frequency Stabilization

Regulating the frequency of our laser cooling beams is vital for our experiment. We have verified our capability to stabilize the Ti:Sapph laser frequency using a digital PID controller. Our locking system relies on a high-precision wavemeter along with LabVIEW software for laser control developed by Kendall Rice '25. As described in her thesis [1], this program applies PID control theory to tune and lock lasers to target frequencies with high precision and accuracy.

Motivating PID Control

Our wavemeter, a Bristol Instruments Model 871A, which we use to measure laser frequency in real time, can resolve laser frequency differences on the 1 MHz scale [1]. Knowing just this live measurement and the set point, one might devise a simple control system to regulate laser frequency. The difference between these two quantities (live frequency - desired frequency) is defined as the error signal. A correction signal proportional to the magnitude and in a suitable direction relative to the error signal could be sent back to the laser to make adjustments toward the desired setpoint. However, this simple control model typically causes the frequency to overshoot the set point and oscillate around the desired frequency instead of settling on it.

A PID system overcomes this issue by incorporating into the correction signal integrated (I) and derivative (D) terms in addition to the rough correction signal proportional (P) to the error signal. The integrated term improves stability by increasing the correction signal if the error signal has been large in magnitude for a long time. The derivative term, which is more relevant for rapidly changing systems, also helps the system converge at the set point by predicting future error based on the current rate of change and correcting for it. For example, if the laser frequency is too high and plummeting towards the set point, the derivative term will be high in magnitude but negative. Therefore, it will counter the positive contributions from the P and I terms to dampen the magnitude of the correction signal, informing the laser that it is overcompensating and will likely overshoot the set point.

Locking the Ti:Sapph

After configuring the reference cavity and the Ti:Sapph's control electronics, we fiber-coupled around 1 mW of the Ti:Sapph's output and delivered it to the wavemeter to supply live wavelength measurements. In the absence of PID control, the wavelength seemed susceptible to drifts on the order of 100 MHz. When PID control was applied, the stability of laser frequency was much improved with a RMS frequency noise of approximately 1.685 MHz (Figure 3.13).

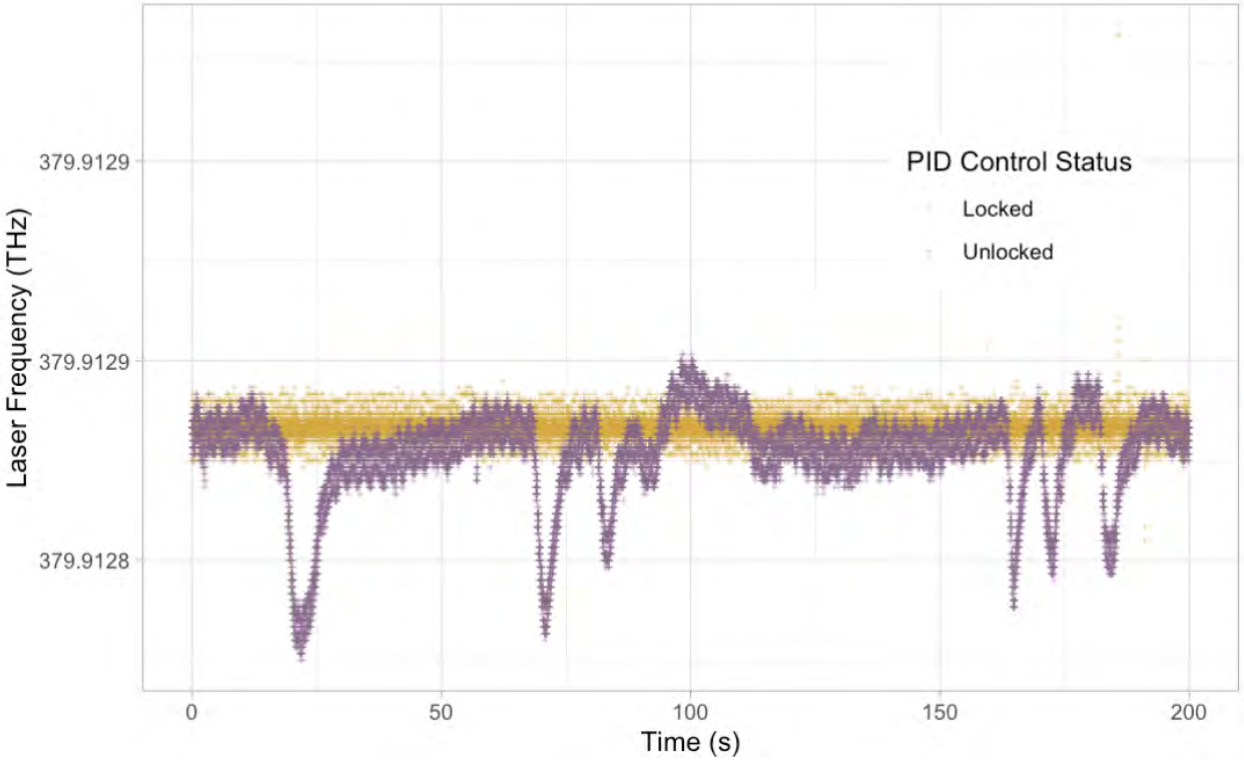

Figure 3.13: Comparison of Ti:Sapph laser frequencies with and without frequency control. The unlocked data is represented by the purple points, while the locked data is represented by the yellow points. Each time step on the x-axis represents 10 ms.

3.3.3 Doubling Crystal Tests

We have ordered and obtained for our bow-tie cavity a 6x4x10mm lithium triborate (LBO) crystal cut for second harmonic generation of 755.2 nm to obtain 378.6 nm and Brewster cut on both ends to minimize loss.

The dimensions of our new crystal were selected to match those of the aged crystal in our cavity. Calculating the phase matching angle for second harmonic generation is challenging and easier done using SNLO software [38]. However, Brewster's angle can be calculated from the Sellmeier equation, which relates the refractive index of a material to the wavelength of light incident upon it. The Sellmeier equation for the n_x principal axis in LBO is

$$n_x(\lambda) = \sqrt{2.4517 - \frac{0.01177}{0.00921 - \lambda^2} - 0.00960\lambda^2}$$

[39].

The laser light propogates from free space into the crystal. Therefore, Brewster's angle for a given wavelength is just the inverse tangent of $n_x(\lambda)$. Doing this calculation yields 57.517°.

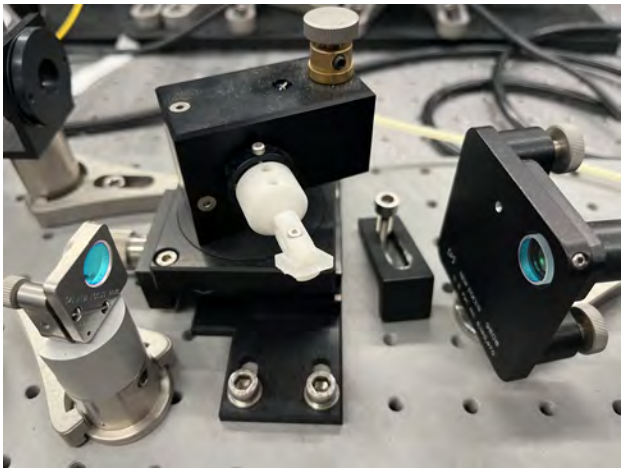

(a) Photograph of the old LBO crystal in our bow-tie enhancement cavity.

(b) Dimensions of our new LBO doubling crystal.

With our locking method established, we plan to stabilize the Ti:Sapph output wavelength at 756 nm and pass it once through our new doubling crystal to verify that we can generate second-harmonic light at 378 nm.

Chapter 4

Future Work

The work presented in this thesis reflects the growing role of tabletop experiments in addressing fundamental questions in physics. For these experiments, the ability to assemble, control, and precisely measure increasingly complex systems, such as molecules and heavy atoms, will be instrumental to probing symmetry-violating effects. Our work marks improvement upon existing molecular and atomic experimental platforms. In the case of DyO, the development of a hyperfine-resolved spectroscopy apparatus with electric field control and completed set of spectroscopic studies represent a significant step toward investigating new physics in a molecule with enhanced sensitivity. Progress toward laser cooling of atomic lead addresses a novel system, expanding the range of species available for precision control and measurement. Building on these advances, future work will extend these techniques in order to achieve greater experimental precision, explore new candidate systems, and ultimately improve sensitivity to BSM physics.

4.1 High-Precision Spectroscopy of Diatomic Molecules

A direction of continuing work on the molecular spectroscopy apparatus focuses on additional spectroscopic studies of DyO. In particular, the excited [18.0]9, [18.5]9, and [19.0]9 states all appear promising for optical cycling [18]. As we completed with the [17.1]7 $\leftarrow$ X8 transition, we seek to elucidate the hyperfine structure of the transition. We will also pursue measurements of the electric dipole moment with our newly-installed electric field plates.

The molecular spectroscopy apparatus has also recently enabled the first observation and characterization of gold carbide (AuC) molecules [40]. AuC is one of the metal-containing diatomic molecules identified as a viable platform for precision measurements to set bounds on the eEDM. As with DyO, we will pursue high-resolution studies of the hyperfine structure and electric dipole moments in the low-lying electronic states of AuC. As AuC is a new system, much remains to be understood to decipher the features of complex spectra. We have already encountered spectra that are difficult to analyze due to the presence of closely-spaced peaks. Our electric field plates can aid in the identification of peaks, since energy levels in the presence of an electric field split into a number of sublevels that is directly related

to the total angular momentum of the state. For a given J (total angular momentum), $2J+1$ Stark levels are formed. Therefore, by collecting Stark-shifted spectra and and observing how peaks split under an applied electric field, we can assign J values to the transitions.

4.2 Demonstration of Transverse Cooling in a Lead (Pb) Atomic Beam

While the output power from the Ti:Sapph has improved following the replacement of the upper fold mirror, our maximum observed power of roughly 400 mW of single-frequency radiation with 12 W of pump power still falls short of expectations. One avenue for improving the output power would be a more comprehensive examination of the Ti:Sapph optics. Thus far, we have measured only the reflectances of the lower and upper fold mirrors, since we concluded our tests after identifying the issue with the upper fold mirror. After inserting the ICA and scanning Brewster plate, we retained only around 40% of the output power, significantly less than the expected 60%, motivating further investigation of these two optics in particular. Another open question is whether the Ti:Sapph crystal is still functioning at full capacity. In addition, the Ti:Sapph is highly sensitive to the alignment of each optic, so it remains possible that suboptimal alignment is negatively affecting the output power.

Even without the output power we desire, it is possible to begin testing the non-linear crystal and bow-tie cavity optics. A scheme for checking the proper function of the non-linear crystal would be locking the Ti:Sapph wavelength to 756 nm, the wavelength that the original doubling cavity and our new crystal was cut for, and passing the light through the crystal once. Tuning the incident angle of light should eventually produce a detectable amount of second harmonic light detectable by a PMT with the installation of dichroics to filter out the fundamental frequency light. The 756 nm light from the Ti:Sapph can also be used to test the reflectances of the mirrors in the bow-tie cavity. Ultimately, realizing our experimental plan will require restoring the full functionality of the bow-tie cavity at 756/378 nm and adapting it for our shorter wavelength application at 736/368 nm. In addition, outside of the laser system, while the atomic beam has already been modified and repurposed for lead (Pb), a fluorescence detection region to image the cooled beam will need to be designed and constructed within the vacuum chamber. Collection optics similar to those used in the molecular spectroscopy apparatus could then be implemented in this region for DLIF detection.

Appendix A

Motor Control Box

The metal target used during molecule synthesis is rotated by an Oriental Motors stepper motor controlled by an accompanying driver. The motor driver, an Oriental Motors model CRD507-KP, is programmable and compatible for computer communication through an RS-485 cable. The timing for rotating the motor is set in a LabVIEW program, which interfaces with a PBJ-based event generator that outputs high-speed, precise 100 MHz event pulses or signals to direct the driver to turn the motor. The event generator, the PBJ1590BB produced by the Harvard electronics shop, produces 5V digital signals at 8 BNC ports. However, the motor driver requires 24V cues delivered in a rainbow ribbon cable (RRC) to rotate the motor. Therefore, we need to convert between 5 V and 24 V signals in order to control the motor with our computer. The motor control box encloses the electronic circuits responsible for converting and delivering input and output signals to and from the stepper motor. It has the capacity to transmit four input signals and four output signals through BNC cables.

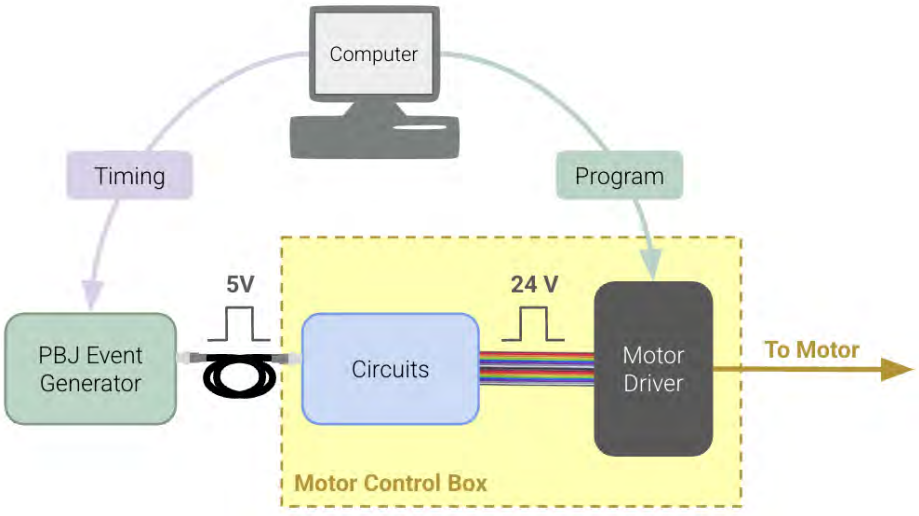

Figure A.1: Schematic of the signaling process for the rotation and translation of the metal sample with a stepper motor.

For daily use, connect the RS-485 communication cable (located to the left of the on/off switch) to the computer serial port and plug the 24 VDC adapter (located on the back of the box) into a power outlet. Flick the switch to on (up) to send power to the motor driver.

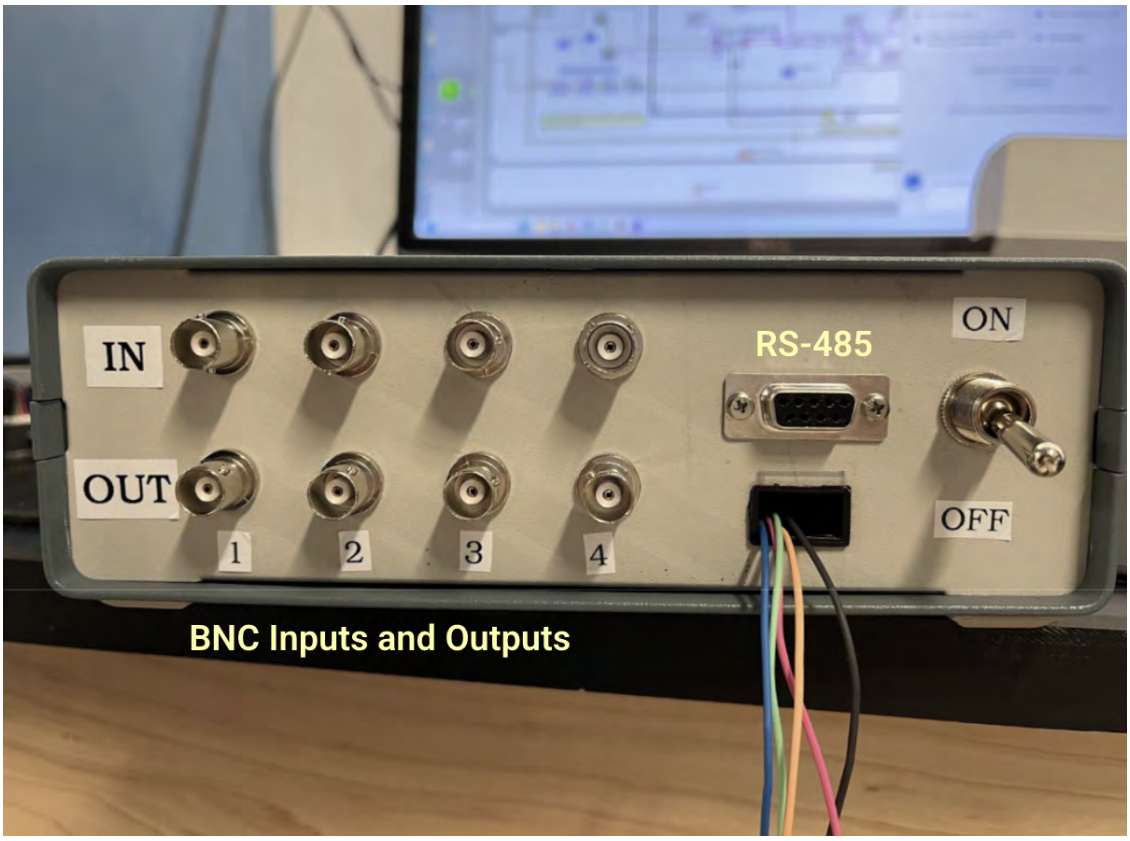

Figure A.2: Front-side view of motor control box.

A.1 Interior Electronics

When a 5V input from the PBJ-based event generator enters the motor control box, it travels through terminal strip 1 to the input of an opto-isolator, which amplifies the 5 V signal into a 24 V signal. The opto-isolator performs the conversion by using the input signal to light an LED, then using a phototransistor to transform the optical signal back into an electrical signal [41]. The opto-isolator requires a 24 V reference to set the voltage of the output. This 24 VDC reference is adapted from a wall outlet. Our opto-isolator chips each have two inputs. Therefore, to convert our four BNC inputs, we use two opto-isolator chips. The 24V signals from our opto-isolator chips are sent through terminal strip 2 to the corresponding RRC inputs destined for the motor driver. The pin assignments for the RRC are displayed on page 28 of the motor driver's operating manual [42]. While our current application does not require output signals from the motor, the capability to retrieve output

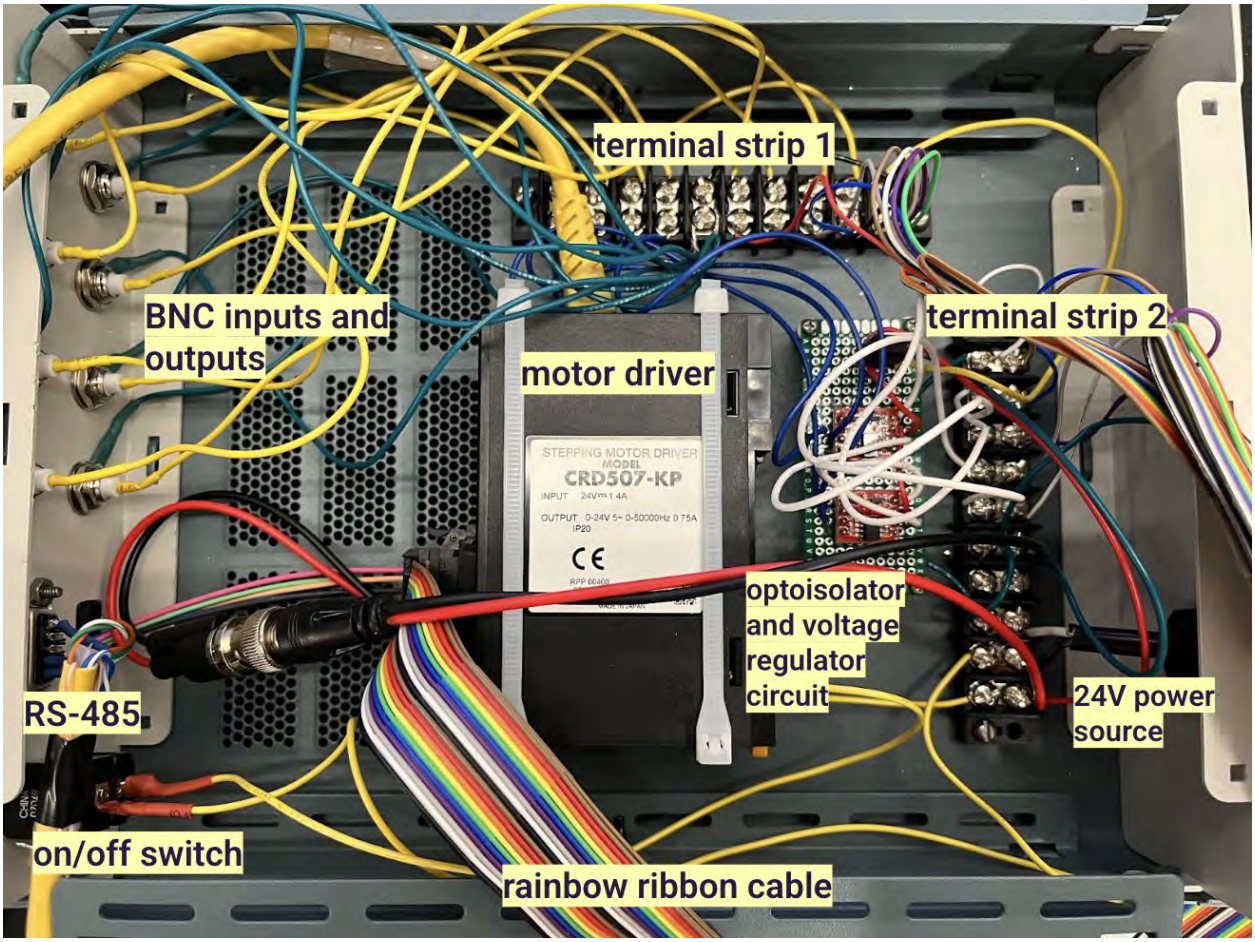

Figure A.3: Overhead view of the interior of the motor control box.

signals in BNC form is built in. The motor driver uses differential signaling for outputs. To ensure that the output signals sent to the computer from the motor driver are no greater than 5V, we tie the positive output pins of the motor driver to a steady 5V signal. This signal is provided by a 5V voltage regulator, which maintains a 5V output given a higher input voltage (the 24V power supply in our case). The regulator and two opto-isolator chips are soldered onto a breadboard that is mounted next to the motor driver.

Opto-isolator and Regulator Breadboard

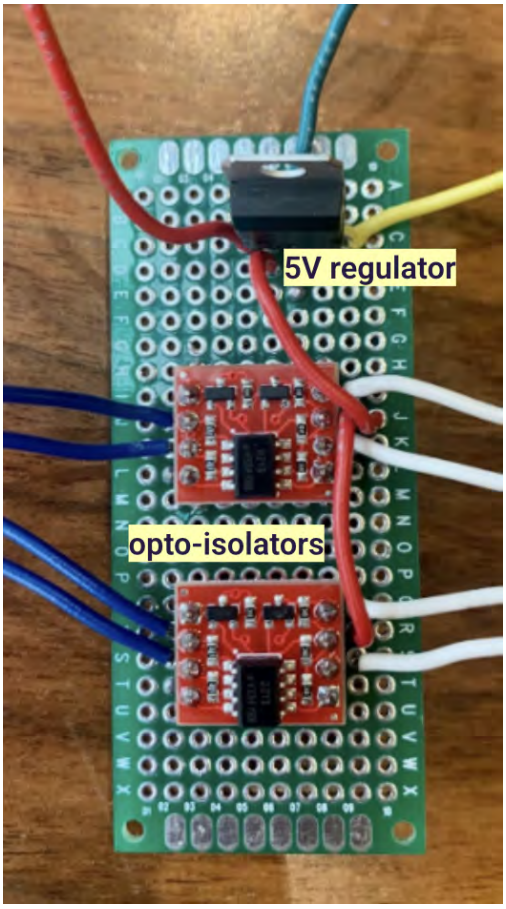

Figure A.4: Top view of the opto-isolator and 5V regulator breadboard.

The red wires connect the 24V power source to the high voltage terminals of each opto-isolator, and the regulator input. The green lead wire attached to the regulator's ground is connected to the grounds of the 24 VDC adapter and the motor control box (and to all other grounds). Grounding wires for the opto-isolators are soldered on the opposite side of the breadboard and therefore not visible in Figure A.4. The yellow wire attached to the regulator's output is connected to the positive outputs of the motor driver. The blue wires on the left side of the breadboard are attached to the inputs of each opto-isolator chip. They are connected to BNC inputs and transmit the 5V input signals to the opto-isolators to be amplified to 24V signals. The white wires on the right side are the outputs from the opto-isolators — the amplified 24V signals from the BNC inputs, which are connected to the inputs of the motor driver.

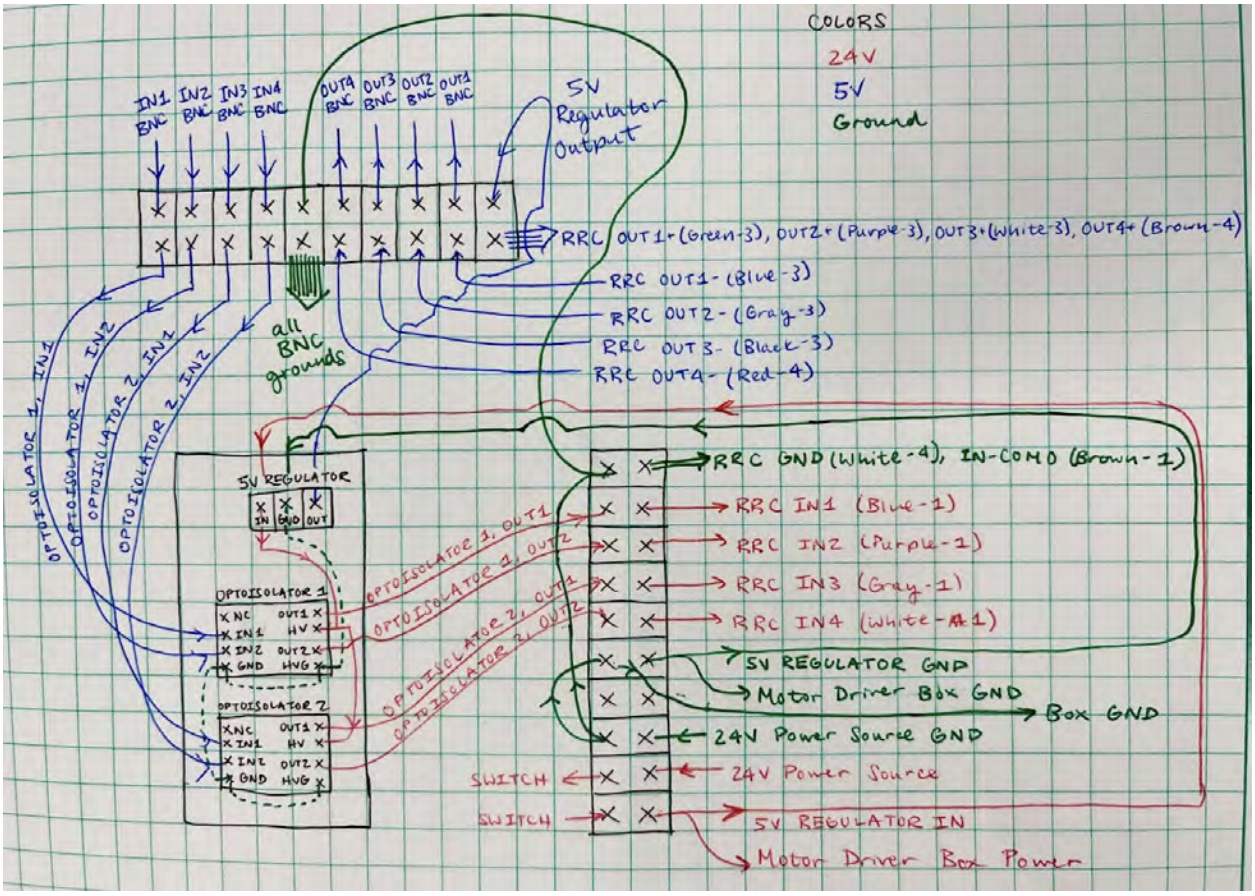

Figure A.5: Connection diagram for the motor control box. Solid lines represent wiring visible from the top and dashed lines represent wiring hidden below. Both terminal strips and the opto-isolator and 5V regulator breadboard are depicted.

Appendix B

Hyperfine Spectroscopy: Experiment Control Code

The synthesis of molecules, the scanning of detection lasers, and the collection of laser-induced fluorescence during high-resolution spectroscopy all occur on microsecond timescales. These processes are synchronized through an NI LabVIEW program that works in conjunction with a laser locking program developed by Kendall Rice '25 and described in her thesis [1]. This appendix documents the program's internal mechanics and provides a guide to accessing the program's features through the user interface.

B.1 Data Collection

Our molecules are produced in periodic pulses. We use a PBJ-based event generator to create cues for the opening of the pulsed valve, firing of the ablation laser, and rotation of the metal sample. This device, the PBJ1590BB produced by Jim MacArthur of the Harvard electronics shop, can send digital signals to 8 channels every 10 ns and is programmed in an accompanying LabVIEW program. After each synthesis cycle, we impose a delay to detect DLIF and tune the probe laser frequency before initiating the next round of molecule production.

The PMT used to detect DLIF at the downstream site releases sharp current pulses when exposed to light from the molecular beam. The current pulses are amplified then digitized by a pulse shaper (also custom built by Jim MacArthur of the Harvard electronics shop) that manipulates the signal into a rectangular pulse shape for processing. This signal conversion mechanism is discussed further in the thesis of Kendall Rice '25[1]. The number of pulses from the PMT within a time frame is summed with the help of the counter input of a National Instruments USB-6212 data acquisition device [43]. We take the the derivative of these totals to derive the count rate as a function of time in the milliseconds following molecule synthesis. To improve the accuracy of our results, we typically go through the experimental cycle (production of molecules and detection of DLIF) multiple times for a given detection laser frequency. We average the count rates at each time point across all

repetitions done with the same detection laser frequency. We then integrate over the time window during which DLIF is detected to obtain a measure of the abundance of counts for a given detection laser frequency. The integration bounds can be adjusted to account for variations in the delay between molecule synthesis and DLIF detection, ensuring that only the true signal is included in the analysis. Our fluorescence spectrum is constructed by compiling these count abundances and allows us to discern DLIF detection levels at a given detection laser frequency relative to other frequencies.

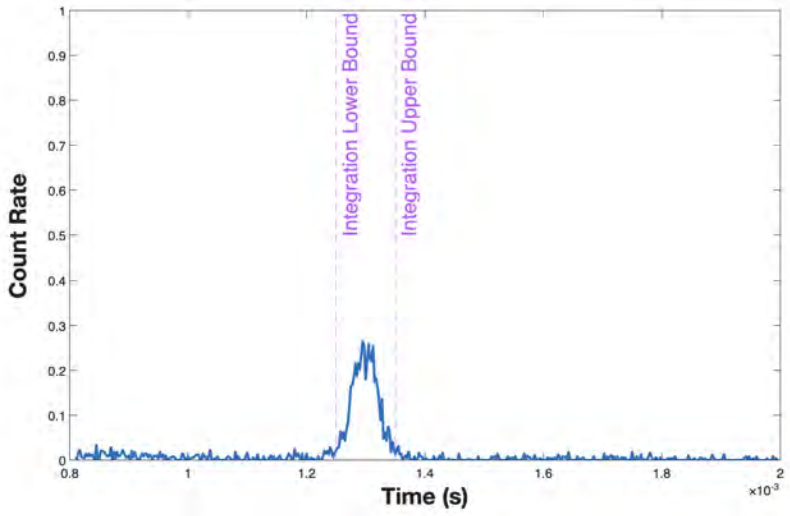

Figure B.1: The time trace is the result of a single repetition. An average of time traces for each frequency is computed and integrated over the time frame containing the DLIF signal (indicated by purple dashed vertical lines) to create a single point on a spectrum.

B.2 Front Panel Daily Use Instructions

B.2.1 Initialization Tab

Prior to initiating data collection, confirm which channels of the NI USB-6212 device are used for which features using the DAQmx Inputs typedef, located in the Initialization tab of the front panel. The current selections are displayed in Figure B.2 and should not require modification from day to day.

Figure B.2: The DAQmx Inputs typedef in the experiment control code allows users to designate which channels of the NI USB-6212 data acquisition device are used for different functions.

Multiple channels can be used to read voltage. This is indicated with, for example, Dev1/ai0:1, which tells the LabVIEW program to read from the ai0 and ai1 channels. The default channel for "Counters" should be Dev1/ctr0. If this option does not appear in the drop down menu, it can be entered manually.

Update the desired parameters for data acquisition using the Data Collection typedef, which is also located in the initialization tab.

Figure B.3: The Data Collection typedef in the experiment control code allows users to set parameters for data collection.

The relevant parameters in this typedef are described below:

- Sample Rate: in Hz, rate at which samples are collected
- Trace Duration: length of each repetition, in ms. When multiplied with the sample rate, indicates how many samples to collect per repetition.
- # of Conditions: number of conditions to test
- Max Shots: when the laser is not scanning, the maximum number of repetitions to collect
- Rep Rate (Hz): not used in data collection, but stored as a parameter when data is saved

B.2.2 Data Collection and Display Tab

If the laser is being scanned, update the Scan Parameters typedef to the desired settings.

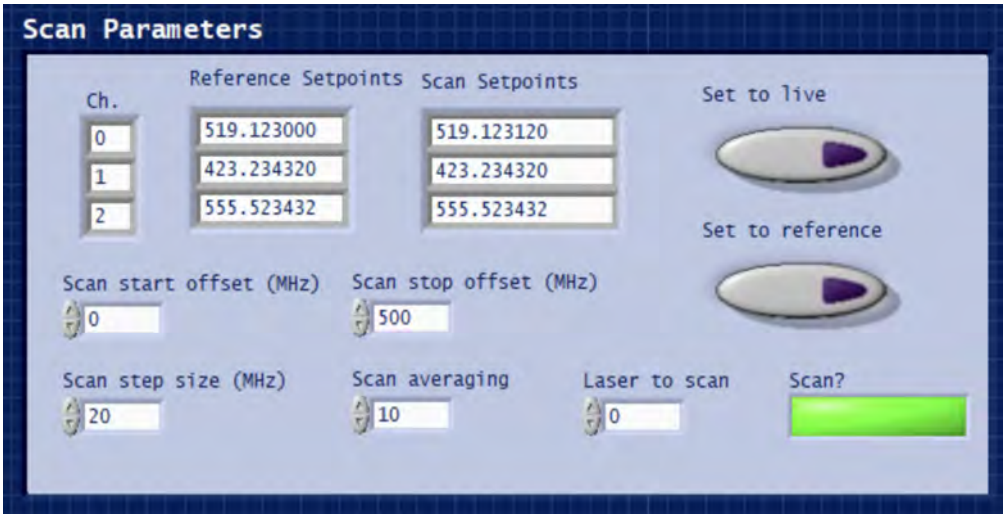

Figure B.4: The Scan Parameters typedef in the experiment control code allows users to manage the scanning of three detection lasers.

The functions of the settings and buttons are explained below:

- Scan?: when true, laser is scanned (updated to the Scan Setpoint). Button appears purple when false, green when true.
- Scan Setpoints: in THz, frequency at which laser is set to.
- Reference Setpoints: in THz, constant changed manually.
- Set to reference: when clicked, sets the Scan Setpoints to the reference setpoints
- Set to live: when clicked, sets the Scan Setpoints to the live frequencies read from our wavemeter and accessed by communication through a notifier feature with laser locking code developed by Kendall Rice [1].
- Scan start offset (MHz): relative to the scan setpoint, where the laser should begin scanning
- Scan stop offset (MHz): relative to the scan setpoint, where the laser should stop scanning
- Scan step size (MHz): how much the laser frequency should increment when going between the start and the end (how much to change the laser frequency between each scan point)
- Scan averaging: number of repetitions to take at each scan point)
- Laser to scan: indicates which laser is being scanned

If you would like the data to be saved, click the Save Data button so that it is green, and type the path for the storage folder into the Path control. Save Last Dataset can also be invoked after data collection even if Save Data is not pressed prior to collection. Data collection is initiated and terminated using buttons at the top of the front panel. When Start Data Collection is clicked, the timestamp will update and the program will begin acquiring data through datacollection.vi. The progress bar and scan state should update as the program progresses through the scan. Clicking Stop Data Collection will end data acquisition regardless of whether all data points have been collected.

During data acquisition, individual time traces (repetitions) are shown in the graph, allowing for monitoring of time traces in real time. The Linear Combinations panel on the right side of the front panel allows users to change the data displayed on each graph.

In the panel, averages indicates the number of repetitions to average. If integer n is entered, the program will average the last n repetitions. Column 1 designates the voltage channel to read, column 2 designates the condition number to read, and column 3 designates how much to weigh the data. Note that this program uses zero-based numbering, meaning that what appears to be row 1 of the array should be referred to as row 0. Therefore, data read into the first row of an array is accessed using index 0, which is relevant for both channel and condition number. To plot multiple sets of data on the same graph, navigate to a new page by incrementing the uppermost index display (starred in Figure B.5).

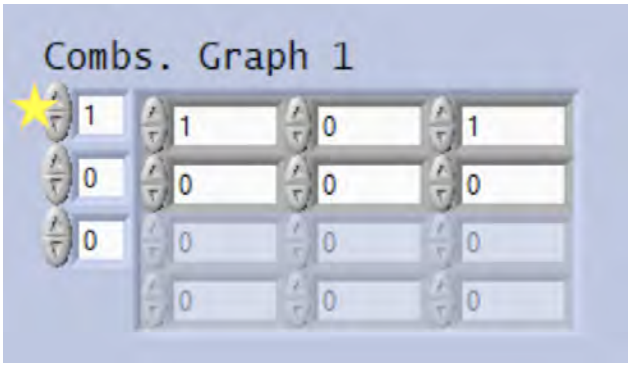

Figure B.5: These settings of the Linear Combinations panel plot data from the first condition of the second voltage channel on the second plot of graph 1. Incrementing the starred quantity allows users to plot multiple sets of data on the same graph.

The Conditions panel can also be modified to introduce basic data processing functions to the graphs. These include as background subtraction, normalizing, integrating, filtering after linear combinations.

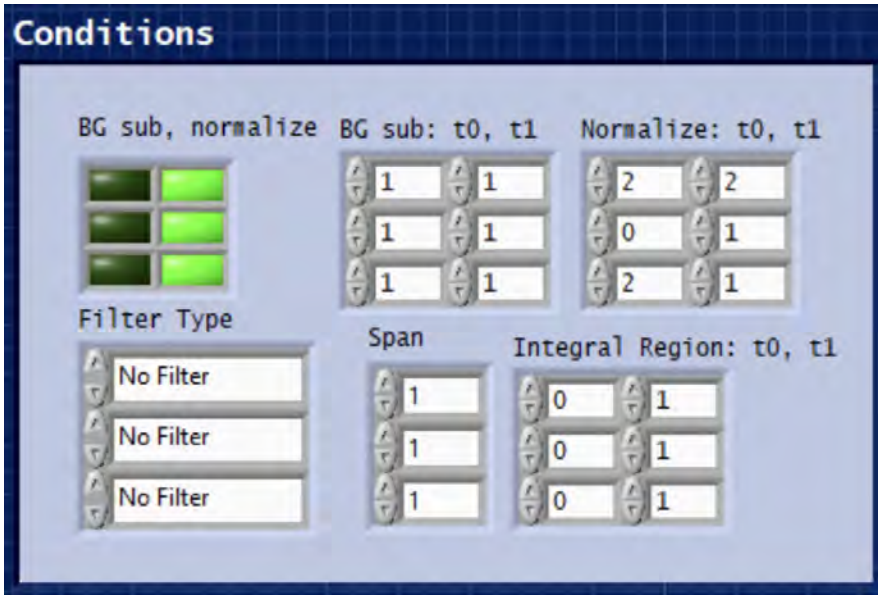

Figure B.6: The Conditions panel manages data processing after linear combinations for display on front panel graphs during data acquisition. With these settings, normalization is turned off and background subtraction is turned on.

For all functions, the first row corresponds to graph 1, the second row corresponds to graph 2, and the third row corresponds to graph 3. Background subtraction and normalization are switched on by clicking on the LEDs to turn them on. For background subtraction, t0 and t1 are used to find the background to subtract: the program takes the mean of the data points between t0 and t1 and subtracts that value from every data point. For normalization, t0 and t1 are used to determine the region of the data to normalize with t0 as the lower bound and t1 as the upper bound. For integration, t0 and t1 are used to determine the region of the data to integrate over.

Appendix C

Ti:Sapph Laser

This appendix describes further details on the operation and alignment of the Ti:Sapph laser, which we use as the source for a second-harmonic generation process to produce ultraviolet light for laser cooling.

C.1 Principle of Operation

The gain medium in the Ti:Sapph is a titanium-doped sapphire (Al_2O_3) crystal with a TiO_3 doping concentration of roughly 1% by weight. The titanium atoms replace aluminum atoms at some sites in the crystal lattice and behave as Ti^{3+} ions. Each Ti^{3+} ion has a single 3d electron available for laser gain, and the electronic states it can occupy are confined to two groups, ^2E and $^2T_2$, each of which contains a high number of vibrational levels. The electronic states are strongly coupled to the distance from titanium atom to oxygen atom in the crystal lattice, so a potential energy diagram can be drawn as a function of this separation [37] .

The Ti:Sapph effectively operates as a four-level laser system. When pump light of around 532 nm is turned on, there will first be a transition from the ground state of $^2T_2$ to an excited vibrational state in ^2E. This occurs due to the Franck-Condon principle, which mandates that the intranuclear distance of a molecule remains fairly consistent during an electronic transition — the distance between titanium and oxygen remains roughly unaltered during this initial electronic transition. Then, rapid thermalization on the scale of picoseconds occurs, yielding a high population in the upper laser level near the bottom of ^2E. The laser transition occurs between this level and a vibrationally-excited level in $^2T_2$. Afterwards, rapid thermalization occurs again and the original ground state is recovered. The speed of thermalization allows for the population inversion between the upper and lower laser levels.

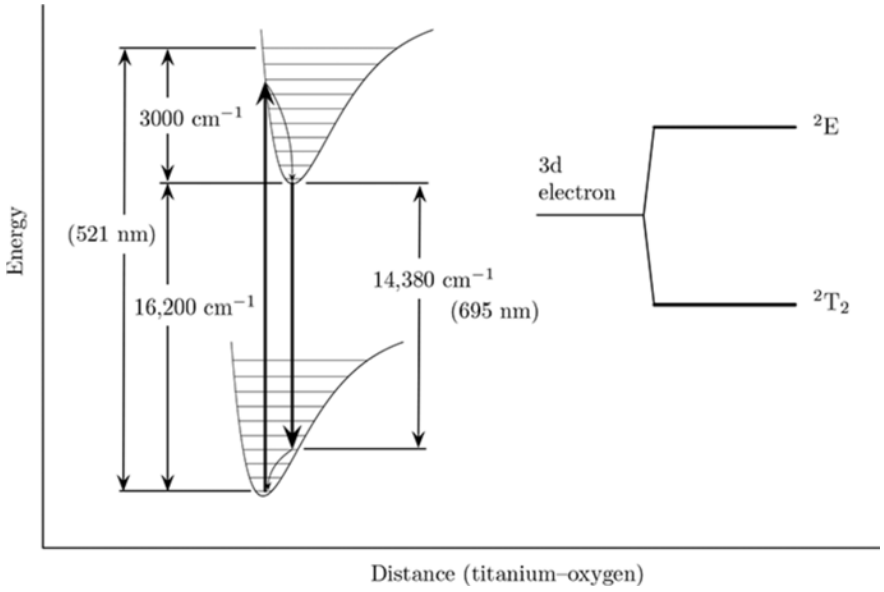

Figure C.1: Energy levels of titanium ions in sapphire crystal. Extracted from [37]

C.2 Coherent-899 Alignment Procedure

The operator's manual provides step-by-step instructions for installing the elements one at a time. After each new optic is added, the manual outlines tests to make sure it is properly positioned. These tests typically involve measuring separation between optical elements and precisely checking the locations of reflections and spots. The basic order of operations in the alignment process is as follows:

1. Starting with low levels of pump light, send the pump beam through the empty laser body and adjust the laser's position until it is level and the center axis is aligned with the pump beam.

2. Install and align various optics: P1, P2, P3, L1, M1, M5. M2/M3 and M4 should already be installed.

3. Insert and carefully position the Ti:Sapph crystal. Connect water cooling tubes to prevent the crystal from overheating. In this step, the pump beam should be incident on the crystal's entry face at Brewster's angle to minimize reflections. A detail not explicitly mentioned in the manual is that since Brewster's angle only exists for light polarized parallel to the plane of incidence, the polarization of the pump laser is not trivial. We insert a half-wave plate into the pump beam's path before P1 and rotate it to adjust the polarization, visually identifying the position that results in the least reflection from the crystal face.

4. Increase the power of pump light to normal operation levels. This should cause infrared light produced by the crystal to become visible. Use a white card to align the infrared

light through the optical diode and translation rhomb to the output coupler M4, and also to position the light through the birefringent filter to the output coupler M4.

5. Adjust the position and focuses of P1, M1, M3 and M4 to accomplish multimode oscillation without the intracavity assembly (ICA) or Brewster plate installed. Monitor and maximize output power by fine-tuning the placement of these optics.

6. Add the ICA, then recover and re-optimize oscillation.

7. Insert the scanning Brewster plate and recover and re-optimize oscillation once again.

8. Configure the reference cavity and control electronics.

Bibliography

[1] K. L. Rice, Bachelor's Thesis, Williams College (2025).

[2] J. Uri, *240 years ago: Astronomer william herschel identifies uranus as the seventh planet* (2024), URL https://www.nasa.gov/history/240-years-ago-astronomer--william-herschel-identifies-uranus-as-the-seventh-planet/.

[3] J. Uri, *175 years ago: Astronomers discover neptune, the eighth planet* (2021), URL https://www.nasa.gov/history/175-years-ago-astronomers-discover-neptune-the-eighth-planet/.

[4] F. Education and P. Engagement, *Muons and other fundamental particles*, URL https://education.fnal.gov/muons-and-other-fundamental-particles/.

[5] G. Altarelli, in *Encyclopedia of Mathematical Physics*, edited by J.-P. Françoise, G. L. Naber, and T. S. Tsun (Academic Press, Oxford, 2006), pp. 32–38, ISBN 978-0-12-512666-3, URL https://www.sciencedirect.com/science/article/pii/B0125126662000596.

[6] D. DeMille, J. M. Doyle, and A. O. Sushkov, Science **357**, 990 (2017), https://www.science.org/doi/pdf/10.1126/science.aal3003, URL https://www.science.org/doi/abs/10.1126/science.aal3003.

[7] G. Gabrielse, Physics Today **66**, 64 (2013), URL https://physicstoday.aip.org/quick-study/the-standard-models-greatest-triumph.

[8] D. J. Griffiths, *Introduction to Electrodynamics* (Cambridge University Press, 2023), 5th ed.

[9] G. Bertone and D. Hooper, Rev. Mod. Phys. **90**, 045002 (2018), URL https://link.aps.org/doi/10.1103/RevModPhys.90.045002.

[10] G. R. Blumenthal, S. M. Faber, J. R. Primack, and M. J. Rees, Nature **311**, 517 (1984), URL https://doi.org/10.1038/311517a0.

[11] T. D. Lee and C. N. Yang, Phys. Rev. **104**, 254 (1956), URL https://link.aps.org/doi/10.1103/PhysRev.104.254.

[12] C. S. Wu, E. Ambler, R. W. Hayward, D. D. Hoppes, and R. P. Hudson, Phys. Rev. **105**, 1413 (1957), URL https://link.aps.org/doi/10.1103/PhysRev.105.1413.

[13] E. Siegel, *The "strong cp problem" is the most underrated puzzle in all of physics* (2019), URL https://www.forbes.com/sites/startswithabang/2019/11/19/the-strong-cp-problem-is-the-most-underrated-puzzle-in-all-of-physics/.

[14] M. S. Safronova, D. Budker, D. DeMille, D. F. J. Kimball, A. Derevianko, and C. W. Clark, Rev. Mod. Phys. **90**, 025008 (2018), URL https://link.aps.org/doi/10.1103/RevModPhys.90.025008.

[15] Nature Physics **22**, 497 (2026), URL https://doi.org/10.1038/s41567-026-03278-4.

[16] D. Pan, H. Xu, and F. J. G. de Abajo, Science Advances **7**, eabd6705 (2021), https://www.science.org/doi/pdf/10.1126/sciadv.abd6705, URL https://www.science.org/doi/abs/10.1126/sciadv.abd6705.

[17] J. E. Kim and G. Carosi, Rev. Mod. Phys. **82**, 557 (2010), URL https://link.aps.org/doi/10.1103/RevModPhys.82.557.

[18] Z. D. Lasner, A. T. Ohl, N. M. Albright, K. L. Rice, C. Peng, L. Cheng, J. M. Doyle, and B. L. Augenbraun, The Journal of Physical Chemistry A **130**, 513 (2026), URL https://doi.org/10.1021/acs.jpca.5c07797.

[19] K. C. Stuntz, K. L. Rice, L. Cheng, and B. L. Augenbraun, Phys. Rev. A **110**, 042807 (2024), URL https://link.aps.org/doi/10.1103/PhysRevA.110.042807.

[20] C. Brunel, P. Tamarat, B. Lounis, J. C. Woehl, and M. Orrit, The Journal of Physical Chemistry A **103**, 2429 (1999), URL https://doi.org/10.1021/jp983956t.

[21] Q. Yin, Z. Liu, B. Wang, K. Ma, Y. Cai, and Q. Song, Journal of Materials Research and Technology **20**, 950 (2022), ISSN 2238-7854, URL https://www.sciencedirect.com/science/article/pii/S2238785422011632.

[22] C. Linton and B. Simard, jcp **96**, 1698 (1992).

[23] T. Chen, C. Zhang, L. Cheng, K. B. Ng, S. Malbrunot-Ettenauer, V. V. Flambaum, Z. Lasner, J. M. Doyle, P. Yu, C. J. Conn, et al., The Journal of Physical Chemistry A **128**, 6540 (2024), URL https://doi.org/10.1021/acs.jpca.4c02640.

[24] V. V. Flambaum and A. J. Mansour, Phys. Rev. C **111**, 055501 (2025), URL https://link.aps.org/doi/10.1103/PhysRevC.111.055501.

[25] W. B. Cairncross and J. Ye, Nature Reviews Physics **1**, 510 (2019), URL https://doi.org/10.1038/s42254-019-0080-0.

[26] D. Mitra, K. H. Leung, and T. Zelevinsky, Phys. Rev. A **105**, 040101 (2022), URL https://link.aps.org/doi/10.1103/PhysRevA.105.040101.

[27] D. M. Meekhof, P. Vetter, P. K. Majumder, S. K. Lamoreaux, and E. N. Fortson, Phys. Rev. Lett. **71**, 3442 (1993), URL https://link.aps.org/doi/10.1103/PhysRevLett.71.3442.

[28] S. J. Phipp, N. H. Edwards, P. E. G. Baird, and S. Nakayama, Journal of Physics B: Atomic, Molecular and Optical Physics **29**, 1861 (1996), URL https://doi.org/10.1088/0953-4075/29/9/028.

[29] A. Nasir, Bachelor's Thesis, Williams College (2024).

[30] G. Ranjit, N. A. Schine, A. T. Lorenzo, A. E. Schneider, and P. K. Majumder, Phys. Rev. A **87**, 032506 (2013), URL https://link.aps.org/doi/10.1103/PhysRevA.87.032506.

[31] H. J. Metcalf and P. van der Straten, J. Opt. Soc. Am. B **20**, 887 (2003), URL https://opg.optica.org/josab/abstract.cfm?URI=josab-20-5-887.

[32] J. H. Lacy, A. C. Kinney, and P. K. Majumder, Phys. Rev. A **111**, 042808 (2025), URL https://link.aps.org/doi/10.1103/PhysRevA.111.042808.

[33] R. S. Wang, Bachelor's Thesis, Williams College (2024).

[34] D. J. Berkeland and M. G. Boshier, Phys. Rev. A **65**, 033413 (2002), URL https://link.aps.org/doi/10.1103/PhysRevA.65.033413.

[35] B. Klöter, C. Weber, D. Haubrich, D. Meschede, and H. Metcalf, Phys. Rev. A **77**, 033402 (2008), URL https://link.aps.org/doi/10.1103/PhysRevA.77.033402.

[36] R. W. Boyd, in *Nonlinear Optics (Fourth Edition)*, edited by R. W. Boyd (Academic Press, 2020), pp. 1–64, fourth edition ed., ISBN 978-0-12-811002-7, URL https://www.sciencedirect.com/science/article/pii/B9780128110027000102.

[37] W. Nagourney, in *Quantum Electronics for Atomic Physics and Telecommunication* (Oxford University Press, 2014), ISBN 9780199665488, https://academic.oup.com/book/0/chapter/150571651/chapter-ag-pdf/44981214/book_6575_section_150571651.ag.pdf, URL https://doi.org/10.1093/acprof:oso/9780199665488.003.0007.

[38] A. V. Smith, *SNLO Nonlinear Optics Software* (2000-2026), URL http://www.as-photonics.com/snlo.

[39] C. Chen, Y. Wu, A. Jiang, B. Wu, G. You, R. Li, and S. Lin, J. Opt. Soc. Am. B **6**, 616 (1989), URL https://opg.optica.org/josab/abstract.cfm?URI=josab-6-4-616.

[40] R. M. Weldon, D. M. Darling, N. M. Albright, K. L. Rice, P. L. Salerno, K. C. Stuntz, and B. L. Augenbraun, *Elucidating au-c bonding via laser spectroscopy of gold monocarbide* (2026), 2604.04322, URL https://arxiv.org/abs/2604.04322.

[41] R. Paschotta, *Opto-isolators*, RP Photonics Encyclopedia (2019), URL https://www.rp-photonics.com/opto_isolators.html.

[42] Oriental Motor Co., Ltd., *Operating Manual: 5-phase stepping motor unit CRK Series Built-in Controller (Stored Program) Package*, Oriental Motor Co., Ltd. (2024), hP-P024-4, URL https://www.orientalmotor.com/products/pdfs/opmanuals/HP-P024-4.pdf?_gl=1*tj1g34*_ga*ODkxMzA2MTMxLjE3MDg2MzA0MTM.*_ga_VV8FQHSH1R*MTcwOTIzODE0Ny40LjEuMTcwOTIzODE1OS40OC4wLjA.

[43] Oriental Motor Co., Ltd., *User Guide: NI USB-621x OEM*, Oriental Motor Co., Ltd. (2023), URL https://www.ni.com/docs/en-US/bundle/usb-621x-oem-features/resource/372083c.pdf.